energies

MDPI

Article

Reliability Enhancement of a Double-Switch Single-Ended Primary Inductance–Buck Regulator in a Wind-Driven Permanent Magnet Synchronous Generator Using a Double-Band Hysteresis Current Controller

Walid Emar [1,*], Mais Alzgool [1] and Ibrahim Mansour [2]

[1] Energy Engineering Department, Faculty of Engineering Technology, Zarqa University, Zarqa 13110, Jordan; malzgool@zu.edu.jo

[2] Electrical Engineering Department, Faculty of Engineering Technology, Zarqa University, Zarqa 13110, Jordan; imansour@zu.edu.jo

* Correspondence: wemar@zu.edu.jo

Abstract: The wind power exchange system (WECS) covered in this paper consists of a voltage source inverter (VSI), a DSSB regulator, and an uncontrolled rectifier. An AC grid or a heavy inductive or resistive load (RL) can be supplied by this system. The DSSB is a recently developed DC-DC regulator consisting of an improved single-ended primary inductance regulator (SEPIC) followed by a buck regulator. It has a peak efficiency of 95–98% and a voltage gain of $(D\ (1+D)/(1-D)$. where D is the regulator transistor's on-to-off switching ratio. The proposed regulator improves the voltage stability and MPPT strategy (optimal or maximum power-point tracking). The combination of the DSSB and the proposed regulator improves the efficiency of the system and increases the power output of the wind turbine by reducing the harmonics of the system voltages and current. This method also reduces the influence of air density as well as wind speed variations on the MPPT strategy. Classical proportional–integral (PI) controllers are used in conjunction with a vector-controlled voltage source inverter, which adheres to the suggested DSSB regulator, to control the PMSM speed and d-q axis currents and to correct for current error. In addition to the vector-controlled voltage source inverter (which follows the recommended DSSB regulator), classical proportional–integral controllers are used to regulate the PMSM speed and d-q axis currents, and to correct current errors. In addition, a model Predictive Controller (PPC) is used with the pitch angle control (PAC) of WECS. This is done to show how well the proposed WECS (WECS with DSSB regulator) enhances voltage stability. A software-based simulation (MATLAB/Simulink) evaluates the results for ideal and unoptimized parameters of the WT and WECS under a variety of conditions. The results of the simulation show an increase in MPPT precision and output power performance.

Keywords: wind turbine (WT); synchronous generator with permanently enduring magnets (PMSG); double switch SEPIC-buck regulator (DSSB); hysteresis current-mode control; dq-current control; wind power exchange system (WECS)

check for updates

Citation: Emar, W.; Alzgool, M.; Mansour, I. Reliability Enhancement of a Double-Switch Single-Ended Primary Inductance–Buck Regulator in a Wind-Driven Permanent Magnet Synchronous Generator Using a Double-Band Hysteresis Current Controller. *Energies* **2024**, *17*, 4868. https://doi.org/10.3390/en17194868

Academic Editor: Youguang Guo

Received: 19 March 2024
Revised: 2 May 2024
Accepted: 20 May 2024
Published: 27 September 2024

1. Introduction

The transformation of wind energy into mechanical energy is carried out by a wind power exchange system (WECS), with the wind transferred into an electrical machine to produce electricity. Due to several advantages, a permanent magnet synchronous generator, commonly referred to as a PMSG, is traditionally preferred over other electrical machines for use in conjunction with WECS systems. The synchronous generator is particularly well suited for automotive applications due to its many advantages over a conventional electric stimulation generator, including high effectiveness, substantial power density, stable and adjustable output voltage, and good performance in terms of the dissipation of heat.

However, the main problem of WECS is that the efficiency of power transmission in these systems is not fixed and changes with the wind speed. The primary issue is that the maximum power-point tracking (MPPT) method, in which information is extracted from the wind turbine, is affected by variations in wind speed and air density [1].

In this paper, uncontrolled diode rectifiers, a space-vector pulse-width-modulated voltage source inverter (VSI), and a double-switch SEPIC–buck regulator (DSSB) are all used with the wind power exchange system (WECS). This proposed system is then used to transfer the energy to a three-phase RL, or an AC grid connected to the VSI through LCL Kalman filters. The primary goal of this paper is to use the suggested DSSB converter with an MPPT-based hysteresis current-mode control to build better control methods for an effective and dependable grid interface system for a gearless, direct-drive variable-speed wind turbine. Moreover, this paper focuses on several aspects of the modeling and analysis of grid-connected variable-speed wind turbines based on permanent magnet synchronous generators with the suggested DSSB regulator to maximize power extraction from the wind.

The DSSB is a newly implemented SEPIC–buck regulator that features two switches: one for the boosting (enhancing) regime and the other for the bucking (stepping down) regime. This regulator can provide higher voltage gain than other conventional DC-DC regulators (buck, SEPIC, boost, and buck/boost) and with better dynamic properties. The recommended regulator is regulated using the well-known MPPT technique in conjunction with the hysteresis current-control method using a double-hysteresis current-mode controller. The source and load currents of the recommended regulator are independently controlled by these two-hysteresis current-mode controllers. They are also used to concurrently control the switching frequency and ripple in the currents of the DSSB [2].

DSSB performance with the proposed hysteresis current-mode controller and design parameters is extensively studied in [1,2]. Peak efficiency of 95–98% is attained by the recommended regulator with a gain in voltage of $(D\ (1+D)/(1-D)$. The results obtained further demonstrate the good performance of the regulator concerning its minimal rise time, settling time, drift, gain margin, and phase margin, which are, respectively, 0.05 s, 0.2 s, 82 dB at 10^4 rad/s, and 45 degrees at 700 rad/s [1–3].

To effectively maximize the output power delivered to the grid, or the AC load, the MPPT controller tracks the rectified voltage and current, regulates them, and reaches the optimal or the maximum power-point tracking. In this paper, the DC link voltage is adjusted while the DSSB input current is kept constant in the presence of fluctuating wind speeds and transient AC load currents because of using the MPPT with the adaptive hysteresis band current controller [3–6].

The maximum power that the turbine produces may be achieved by adjusting the turbine pitch angle, tip speed ratio, and PMSG electromagnetic torque while using a wind speed sensor to keep track of wind speed. The standard optimum speed of the PMSG is calculated using the observed wind speed. The power and torque of the turbine are calculated using this speed. The rated specifications of the wind turbine and PMSG are used to compute the coefficient of optimum power [3–6].

Furthermore, field-oriented control, known as dq-axis current control, with three classical PI controllers is used to control the dq-axis currents and voltage of the AC grid and load via the voltage source inverter (VSI). Because of their simplicity, PI controllers are the most often used controllers for implementing d-q axis current loops [3–6]. Ziegler–Nichols and a process of trial and error (usually known as the trial–error method) are two of the most popular tuning techniques that are used for determining PI control gains [4–9]. The recommended tuning method is much easier to use and does not require complicated control algorithms. The recommended method also necessitates very little knowledge of the dynamics of the motor. In comparison to most other techniques, particularly machine learning techniques, this control algorithm is very cost-effective because it makes use of simple PI controllers.

According to our simulation results in Simulink/MATLAB 2021a, the proposed WECS with the DSSB regulator and field-oriented VSI is shown to have the potential to enhance long-term voltage stability and speed, as well as the active and reactive powers delivered from the PMSG. Hence, the characteristics of the recommended DSSB regulator are as follows:

1. When operating at the same duty cycle rate, the DSSB regulator provides greater voltage gain than step-up SEPIC regulators and other conventional DC-DC regulators.
2. The comparison study conducted for this work indicates that DSSB is more practical than conventional buck and SEPIC regulators, particularly for high-power renewable-energy systems, electric vehicles, and solar panels.
3. The double-PI hysteresis control approach with the well-known MPPT technique is an additional benefit, which is normally very straightforward for a DSSB regulator structure. This configuration can significantly reduce the level of harmonics generated at the input and output in comparison to the current boost regulators, SEPIC, and bucking/boosting circuits. This leads to a wider output DC voltage range, greater power capacity, greater current rating capacity, and improved efficiency. Consequently, the regulator can reach its maximum power point, which is contingent only upon the mutual multiplication of the input/output DSSB voltages and currents [1,2].

The key contributions of this paper are as follows:

1. According to the comparative and analytical study that is carried out in this paper, DSSB is more practical and has better dynamic performance than other DC-DC regulators, especially for high-power renewable-energy systems, electric vehicles, and solar panels, than the conventional boost regulator.
2. The hysteresis current-mode control of the source and load currents of the DSSB regulator is an additional benefit of this paper. This control technique is normally very straightforward for any double-switch-based DC-DC regulator structure since it includes a dual-hysteresis current methodology with two PI current regulators.
3. The perturb and observe approach (MPPT technique) used in conjunction with hysteresis current-mode control enhances the performance of the field-oriented VSI. This effectively maximizes the output power supplied to the load and helps achieve the maximum power point of the WECS system in different operating conditions.
4. A simulation study is conducted in the environments of Simulink/MATLAB and Ansoft Simplorer to verify the efficacy of the suggested system.

2. Modeling, Analysis, and Control of the DSSB Regulator

The system structure of the WECS-based PMSG with a variable-speed wind turbine (VSWT) is depicted in Figure 1. It uses a diode rectifier, a DSSB regulator, and a voltage source inverter (VSI) to supply a three-phase AC load in the form of an AC RL or AC grid through LCL Kalman filters.

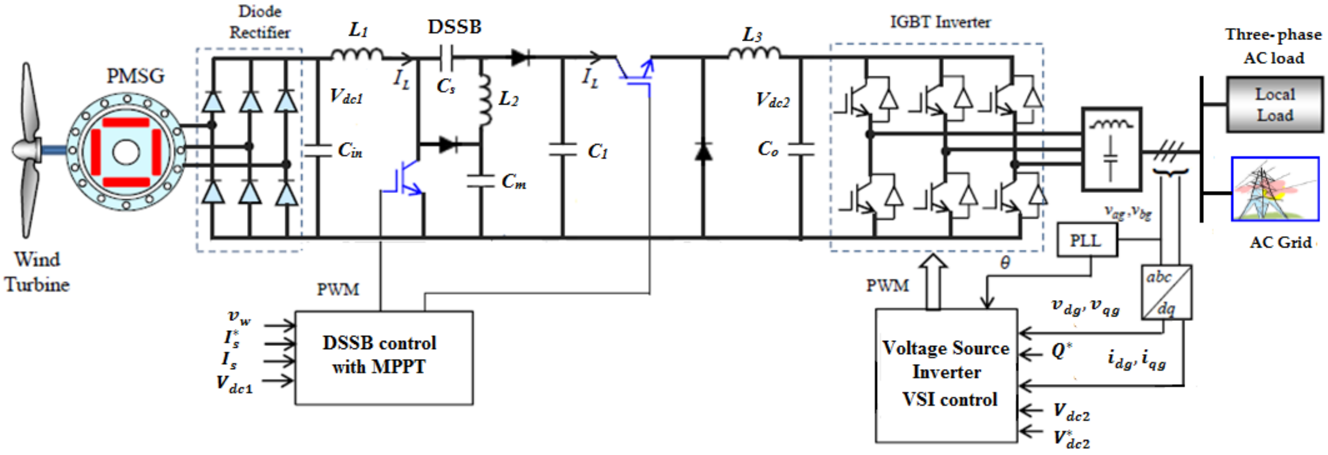

Figure 1. PMSG-based VSWT with a rectifier and boost DC-DC regulator, Voltage Source Inverter (VSI), and PMSM load.

The generator responds to variations in wind speed by altering the amplitude and frequency of its output. The power electronic interface and the controllers provide a controlled voltage and output frequency to power the load. Variable output AC voltage is converted to DC voltage by a diode rectifier; the DC voltage output of the rectifier is then adjusted by a DSSB DC-DC regulator to a level suitable for the inverter operation. To optimize the power extracted from the wind turbine and regulate the output of the switch-mode rectifier, the reference cycle of the DSSB can be adjusted at any wind speed [7–9].

The wind energy system and PMSM are interfaced with the vector-controlled IGBT inverter (grid-side regulator). The output voltage and frequency of a stand-alone system are managed by the grid-side inverter.

The DSSB Regulator

The DSSB regulator shown in Figure 2 is explained in detail in [1,2]. The power electronic switches (MOS1 and MOS2) are used for the boosting and bucking regimes, respectively, in this configuration.

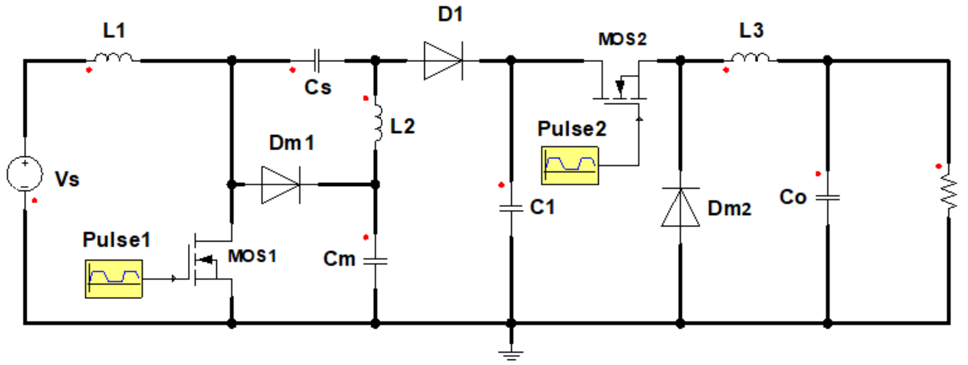

Figure 2. Possible connection of DSSB regulator.

Four capacitive filters (C_s, C_m, C_1, and C_o), three smoothing chokes (L_1, L_2, and L_3), and three diodes (D_{m1}, D_{m2}, and D_1) work together with the two switches of the DSSB regulator to step up and down the DSSB output voltage with very little harmonic content and high power efficiency. In this scenario, the recommended regulator's load is regarded as a DC resistive load.

The fact that the regulator switches are driven by two pulses with the same operating period, T, illustrates the nature of its working principle. The on-time of each switch is DT and $(1-D)T$, respectively. The switches may show a time shift in phase and not be turned on simultaneously, depending on the switching modulation used to achieve the desired voltage at the output. A detailed explanation of the precise behavior and a mathematical analysis of the recommended DSSB regulator are found in [1,2].

The DSSB output DC voltage magnitude and other capacitive voltages are related to the DSSB input DC voltage, V_s, in the following manner, according to the findings in [1,2]:

$$\begin{array}{c} V_{Cm} = \frac{1}{1-D}\,V_s \\ V_{Cs} = -DV_{Cm} = \frac{-D}{1-D}\,V_s \\ V_{C1} = \frac{V_o}{D} \\ V_o = \frac{D\,(1+D)}{(1-D)}\,V_s \end{array} \tag{1}$$

Additionally, when $D = -1 + \sqrt{2}$, the output voltage and supply voltage are equal. Consequently,

$$\frac{V_o}{V_s} = \frac{D\,(1+D)}{(1-D)} = 1 \Longrightarrow D = -1 + \sqrt{2} \tag{2}$$

The volt–ampere simulation waveforms in the bucking and enhancing regimes, respectively, are shown in Figures 3 and 4. These waveforms were detected using the DSSB simulation parameters listed in Table 1. According to Equation (2), DSSB is run in the stepping-down regime for $0 < D < \left(-1+\sqrt{2}\right)$ and in the enhancing regime for $\left(-1+\sqrt{2}\right) < D < 1$.

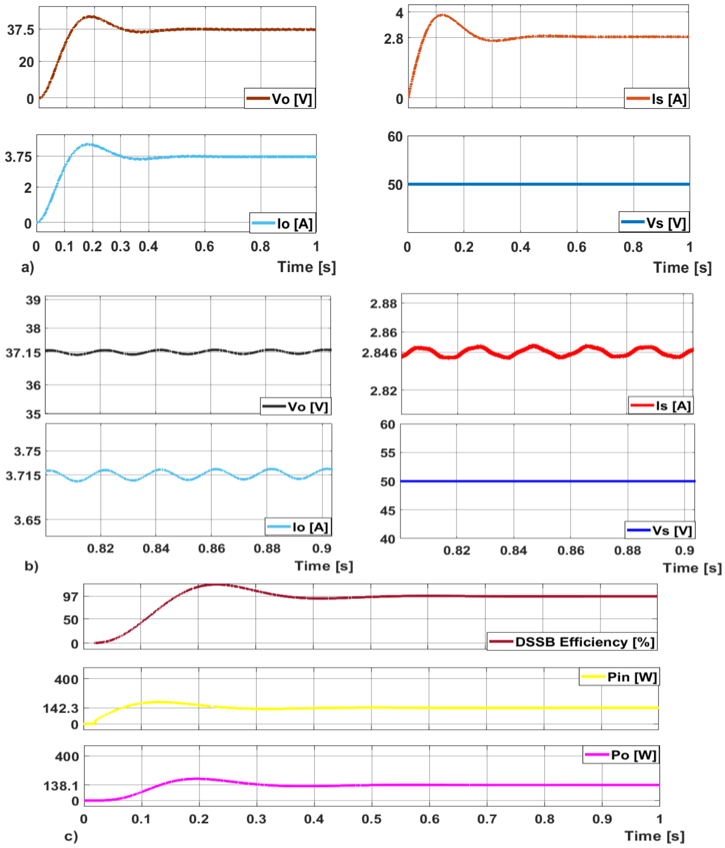

Figure 3. Results of the DSSB MATLAB simulation for $D \leq \left(\sqrt{2}-1\right)$: (**a**) waveforms for the DC voltage and current in the input and output of the DSSB under equilibrium conditions. (**b**) Steady-state waveforms of DSSB currents and voltages. (**c**) DC input and output powers with a regulator efficiency of 99%.

Table 1. QDBC simulation parameters.

Parameter	Symbol	Real Value
Input voltage	V_s	50 V
Input choke	L_1	50 mH
Shunt choke	L_3	50 mH
Output choke	L_2	50 mH
Smoothing capacitor	C_s	1 mF
Shunt capacitor	C_m	470 µF
Shunt capacitor	C_1	470 µF
Output capacitor	C_o	1 mF
Load resistance	R	10 Ω
Switching frequency	f	10 kHz

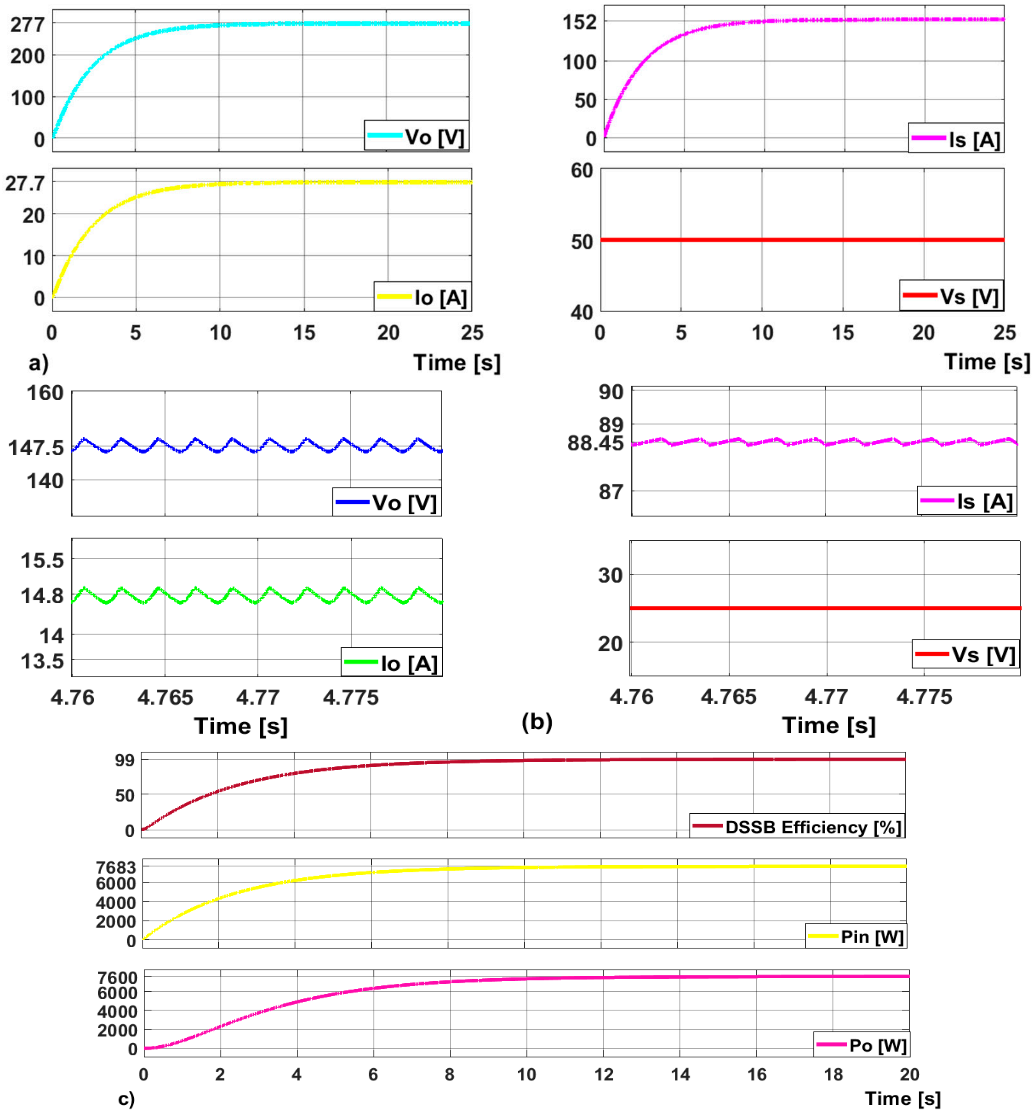

Figure 4. Results of the DSSB MATLAB simulation for $D \geq \left(\sqrt{2}-1\right)$: (**a**,**b**) Waveforms for the steady-state current and voltage in the DSSB for both the input and output DC voltages and currents. (**c**) DC active powers of input and output with a 99% regulator efficiency.

3. Creation of the Equivalent Circuit and Equations for the PMSG Model

Synchronous machines, like most electric machines, can function as both motors and generators. A synchronous machine rotates at a set speed when it is in a quasi-stationary state. In contrast to asynchronous machines, a synchronous machine's rotor and revolving air gap field rotate at the same speed, or at a "synchronous speed".

A synchronous generator with permanently enduring magnets consists of two components: the rotor and the stator. A three-phase synchronous machine stator's distributed winding is comparable to that of a three-phase induction machine. In contrast to a DC machine, the armature winding comprises stator winding that is connected to the AC supply system. Its purpose is to manage elevated voltages and currents.

The rotor carries a permanently enduring magnet or a direct-current-field winding to create a consistent magnetic field within the stator circuit. Figure 5 shows the basic configuration of a synchronous machine [4].

The three windings of the armature circuit are displaced 120° relative to each other and produce three-phase voltages, v_{sa}, v_{sb}, and v_{sc}, that present sinusoidal waveforms at the input terminals [4–8].

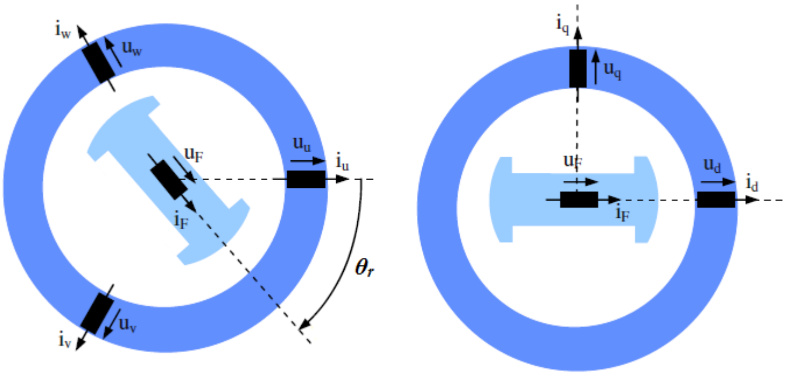

Figure 5. Sketch of a three-phase salient-pole synchronous machine: original system (**left**), and two-phase replacement (**right**).

Essentially, the working principle of the synchronous generator relies on the following equation:

$$n = 120f/p \tag{3}$$

where f is the supply frequency and p is the pole pair of the machine.

Mathematical Model of PMSG

The entire system can be simulated using the PMSG mathematical model. This model is necessary for determining the PMSG's control mechanisms. This model seeks to provide theoretical and analytical solutions to control problems [3–8].

A generator, a rotor shaft, a blade-pitching mechanism with a spinner, and a hub with blades make up the drive train of the variable-speed WECS recommended in this paper. In the wind turbine (WT), the rotor provides aerodynamic torque, while the PMSG provides electromechanical torque. Equation (4) provides the torque values [9–11]:

$$\begin{array}{c} T_m = \frac{P_m}{\omega_r} \\ T_e = \frac{P_e}{\omega_e} = \frac{2}{P}\,\frac{P_e}{\omega_r} \end{array} \tag{4}$$

The typical PMSG mechanical equation is given in Equation (5):

$$J\,\frac{d\omega_r}{dt} = T_m - B\omega_r - T_e \tag{5}$$

where ω_e is the electrical angular frequency of the PMSG, P is its pole number, J is its inertia moment, B is its friction coefficient, and T_m is the mechanical torque of the PMSG.

It is relatively simple to determine the double-phase coordinate reference dq frame based on the ABC real triple-phase frame. When things are running smoothly, the dq frame has direct-current (DC) quantities, whereas the ABC frame has alternating-current (AC) quantities. For control and simulation purposes, the phase coordinate reference dq-frame is therefore frequently used instead of the ABC real triple-phase frame at the reference rotation speed. With the use of mathematical facilitation, linear equations can be obtained. Furthermore, the decoupled control of reactive power and active power in three-phase systems is made simpler by these equations [8].

In the most-used PMSG model, the hysteresis losses, skin effect, magnetic saturation, dampening winding, rotor saliency, and stator core losses are disregarded. The equations for PMSG voltage are expressed as follows [10–12]:

$$\begin{array}{c} v_{ds} = -R_s\, i_{ds} - L_d\, \frac{di_{ds}}{dt} + \omega_r\, \psi_{qs} \\ v_{qs} = -R_s\, i_{qs} - L_q\, \frac{di_{qs}}{dt} + \omega_r\, \psi_{ds} \end{array} \tag{6}$$

The stator voltage, current, and flux of the PMSG are represented by the dq-axis parameters v_{ds}, v_{qs}, i_{ds}, i_{qs}, $\psi_{ds,}$ and ψ_{qs} in the dq reference framework. The stator winding resistance is represented by R_s, while the radian speed of the generator is represented by $\boldsymbol{\omega_r}$.

If the dq axes revolve at the synchronous speed, the stator flux can be computed using the following formula if the d-axis coincides with the rotor flux [4,10–12]:

$$\begin{aligned} \psi_{ds} &= L_d\, i_{ds} - \phi_f \\ \psi_{qs} &= L_q\, i_{qs} \end{aligned} \tag{7}$$

The parameter ϕ_f represents the constant linkage flux value produced by the rotor's permanently enduring magnet and shared by the stator windings. The active and reactive powers of the PMSG can be expressed as follows [10–13]:

$$\begin{aligned} P_{gen} &= \tfrac{3}{2}\left[V_{qs}\, I_{sq} + V_{ds}\, I_{ds}\right] = \tfrac{3}{2}\, V_{ds}\, I_{ds} \\ Q_{gen} &= \tfrac{3}{2}\left[V_{qs}\, I_{ds} - V_{ds}\, I_{qs}\right] = \tfrac{3}{2} V_{ds}\, I_{qs} \end{aligned} \tag{8}$$

L_d and L_q are the dq-axis stator inductances in Equations (6) and (7). Figure 6 shows the dq-model circuit of the PMSG in the synchronous reference frame. Furthermore, the electromagnetic torque is obtained using the subsequent equation in the dq-reference framework [14,15]:

$$\tau_e = \frac{3}{2}\, N_p\, \left(\psi_{ds}\, i_{ds} - \psi_{qs}\, i_{qs}\right) = \frac{3}{2}\, N_p\, \left(\lambda_m\, i_{qs} - \left(L_d - L_q\right) i_{ds}\, i_{qs}\right) \tag{9}$$

where N_p is the number of pairs of PMSG poles. Given that the PMSG is a non-salient pole machine, and that $L_d = L_q$, The electromagnetic torque (τ_e) and the rotor speed (ω_r) of the PMSG are calculated as follows [2]:

$$\begin{aligned} \tau_e &= \tfrac{3}{2}\, N_p\, \left(\lambda_m\, i_{qs}\right) \\ \omega_r &= \tfrac{N_p}{Js}\, \left(\tau_e - \tau_m\right) \end{aligned} \tag{10}$$

where τ_m is the mechanical torque applied to the generator shaft by the turbine, and J is the generator's rotational inertia. Figure 7 displays a simplified schematic diagram of the simulated WECS system, which includes functional blocks of the VSWT and PMSG and is connected to the three-phase grid through a three-phase diode rectifier, a DSSB regulator, a three-phase VSI, and a T-model of the three-phase LCL Kalman filter (transmission line). Power electronic components referred to as MOSFETs are used in this configuration for the generator-side regulator (DSSB) and for the front-loading inverter (VSI) [14,15]. The VSI MOSFETs are modulated using the dq-axis current field-oriented control technique in this paper, while the DSSB regulator MOSFETs are gate-pulsed using the hysteresis current-mode modulation strategy.

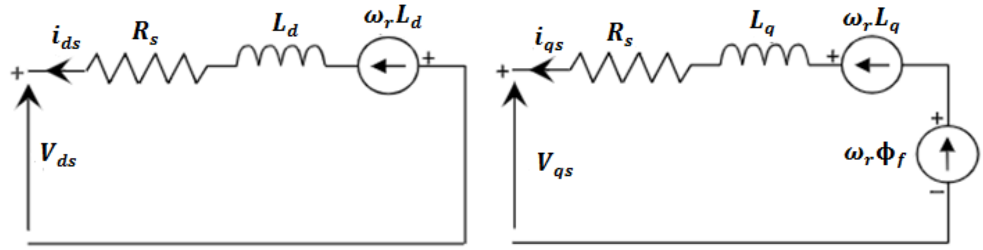

Figure 6. dq model of PMSG equivalent circuit in the synchronous reference frame.

Various control methodologies, including PMW, field-oriented control, hysteresis current-mode control, model predictive-based control, and others, are available for controlling switch-based regulators [14–16]. However, the stationary natural field-oriented control scheme has demonstrated good performance under non-ideal voltage conditions [14]. An

AC small signal control approach that can effectively and dependably handle uncertainties and unidentified disturbances in a DSSB regulator was presented in [16].

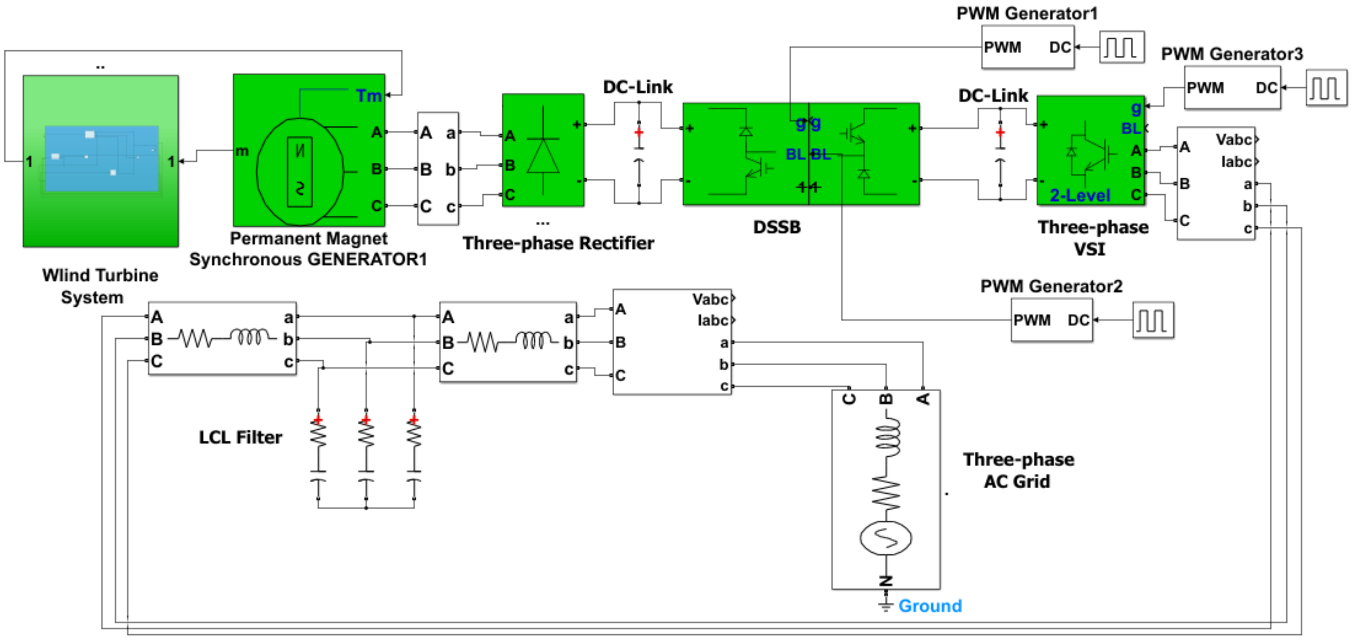

Figure 7. Simplified schematic diagram of the simulated WECS system with an AC grid.

4. Modeling of Variable-Speed Wind Turbine (VSWT)

The wind is a mass of air producing kinetic energy from motion. Naturally, mechanical energy can be produced from this kinetic energy by a VSWT fitted with rotor blades. A PMSG is then used to transform this mechanical energy into electrical energy.

The kinetic energy of wind with a certain mass m and velocity v_w through area A can be found using [14–18]

$$K_E = \frac{1}{2}\, m\, v_w^2 \tag{11}$$

where m is the mass of air in kilograms (kg) and v_w is the wind speed expressed in meters per second (m/s). Given that power is the definition of energy per each spent time unit, the power of a mass of air traveling through an area A at a velocity of v_w for a given time T can be calculated as follows [14–18]:

$$P_w = \frac{1}{2}\,\frac{mass}{time}\, v_w^2 = \frac{1}{2}\,\frac{m}{T}\, v_w^2 \tag{12}$$

Given that the mass flow rate (m/T) is determined by multiplying the airspeed (v_w), cross-sectional area (A), and air density (ρ), Equation (12) can be written as follows:

$$P_w = \frac{1}{2}\,\rho\, A\, v_w^3 \tag{13}$$

where A (m^2) is the sectional region that the wind travels through, ρ is the air density (kg/m^3), and P_w is the power generated by the wind (W). The VSWT converts the wind power generated from air motion into mechanical power via its rotor blades. The rotor's sweeping area, air density, and wind speed all affect how much energy the wind transfers to the rotor [14–18]. Thus,

$$P_T = \frac{1}{2}\,\rho\, A v_w^3\, C_p(\lambda,\ \beta) \tag{14}$$

The turbine rotor power coefficient, or Betz Limit, is denoted by C_p, and it depends on the pitch angle (β) and tip speed ratio (λ). A non-dimensional measure of how well a wind turbine captures energy from a wind stream is the performance (ratio) coefficient C_p. Even when power losses are considered, a wind turbine can only capture 59% of the wind power, as demonstrated by German engineer Betz. The typical (Cp, λ) characteristics of a wind turbine are displayed in Figure 8 [18–20].

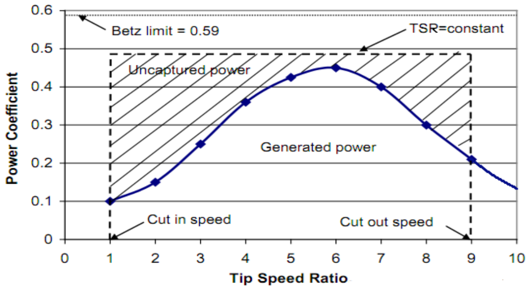

Figure 8. Power ratio (coefficient) versus tip speed.

The performance index of a WT known as the tip speed ratio (TSR) can be found using the following formula:

$$TSR = \lambda = \frac{\omega_m \ R}{v_w} \ \Rightarrow \ v_w = \frac{\omega_m \ R}{\lambda} \tag{15}$$

where R is the radius (in meters) of the turbine, and ω_m is the turbine rotor's mechanical speed (rpm). Following reordering, the turbine power can be expressed as follows:

$$P_T = \frac{1}{2} \rho \ A \left(\frac{\omega_m \ R}{\lambda}\right)^3 C_{opt}(\lambda, \ \beta) \tag{16}$$

Equation (16) demonstrates that when the wind turbine operates at the optimal performance coefficient, indicated by C_{opt}, it can generate its maximum power. Maintaining the rotor speed at the optimal tip speed ratio, λ_{opt}, will guarantee the maximum power extraction from the wind through power-point tracking. The turbine rotor speed needs to be changed whenever the wind speed changes [19–22].

A graph of the dependence of the turbine's mechanical power P_T on the tip speed ratio λ and power performance C_p is shown in Figure 9.

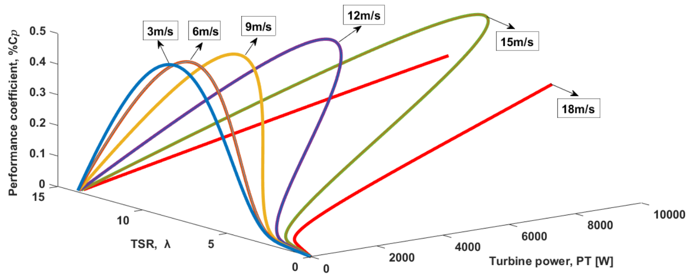

Figure 9. The turbine's mechanical driving power in relation to tip speed ratio and power output at different wind speeds.

Equation (16) can be used to express the optimum mechanical power of the turbine as follows:

$$\begin{aligned} P_{mopt} &= \tfrac{1}{2} \rho \ A \left(\frac{\omega_{mopt} \ R}{\lambda_{opt}}\right)^3 C_{opt} = K_{opt} \ \left(\omega_{mopt}\right)^3 \\ K_{opt} &= \tfrac{1}{2} \rho \ A \left(\frac{R}{\lambda_{opt}}\right)^3 C_{opt} \\ \omega_{mopt} &= \frac{\lambda_{opt}}{R} v_w = K_w v_w \end{aligned} \tag{17}$$

The performance coefficient, which is applied to all wind turbine designs, has an optimal or maximum value of 59.26% [16–22]. However, modern wind turbines function at a somewhat reduced practical non-ideal performance coefficient. For an economically viable wind turbine, a C_p value of 0.35 to 0.40 is a reasonable design target. This is still lessened by an intermittency factor (capacity factor) that considers the times when there is wind flow [18–22].

As a result, to extract the maximum amount of power, the rotor blade must rotate at a frequency proportional to the speed of the approaching wind. Equation (17) shows that the optimal λ_{opt} can be used to characterize this rotor rotational frequency, which decreases as the rotor radius increases [18–22]. Thus,

$$\lambda_{opt} = \frac{\omega_{mopt}}{v_w} R = \frac{2\pi}{n} \left(\frac{R}{A} \right) \tag{18}$$

where n is the number of rotor blades of the wind turbine. To maximize wind power extraction, a wind turbine with fewer rotor blades needs to rotate at a faster speed. Empirical observations indicate that for a rotor with n blades, the swept area A is roughly equivalent to 50% of the rotor radius. Therefore, we establish the following [19–24]:

$$\frac{A}{R} = 0.5 \Rightarrow \lambda_{opt} = \frac{4\pi}{n} \tag{19}$$

When $n = 2$, the optimal λ_{opt} is 6.28; when a rotor has three blades, it is 4.19; and when a rotor has four blades, it drops to 3.14. With the correct airfoil design, the ideal λ_{opt} values could be 25–30% higher. Thus, the incredibly effective rotor blade airfoils increase the rotational speed of the blade, which increases the power production. This suggests that a three-bladed rotor's ideal λ_{opt} would be between 5.24 and 5.45.

The optimal output torque of a wind turbine delivered to the PMSG rotor shaft can be expressed as

$$\tau_{opt} = P_{mopt} / \omega_{mopt} = K_{opt} \left(\omega_{mopt} \right)^2 \tag{20}$$

Equation (20) illustrates how to determine the optimal torque based on the optimal power. The generator operates according to Equation (17) when its operating speed is lower than its rated speed. If the generator's operating speed is higher than the assessed speed, wind turbine's harvesting must be restricted by pitch adjustment or getting the machine to a standstill point [19–24].

The output power of a VSWT fluctuates with its rotation rate for a given wind speed. The ideal power curve, shown in Figure 10, shows the maximum power-point tracking power obtained from the changing wind speed. The controller should be designed to monitor changes in wind speed to ensure that the wind turbine generates the maximum amount of power at any velocity inside its operating range [19–24].

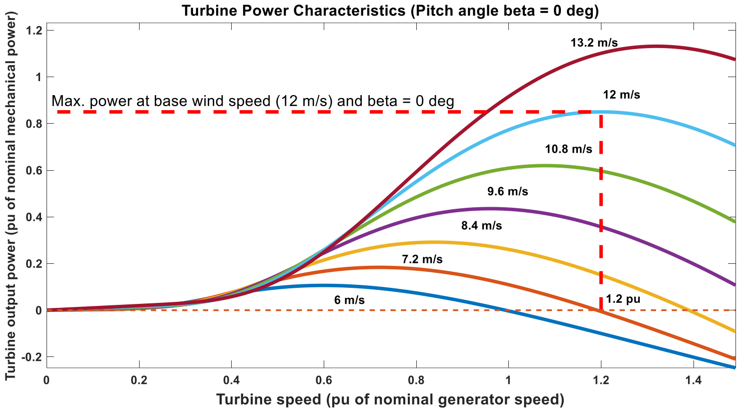

Figure 10. Turbine-generated mechanical power as a function of rotor speed for varying wind speeds.

5. Double-Hysteresis Current Control of DSSB Regulator

As previously mentioned, a three-phase full-wave diode bridge rectifier is used to extract the supply voltage needed for the recommended DSSB regulator from the PMSG. From low- to high-power applications, this rectifier topology is most likely the most widely used. A diagram of the recommended regulator DSSB supplied from a three-phase AC source via a triple-phase diode rectifier and regulated using a double-hysteresis current-mode controller is shown in Figure 11.

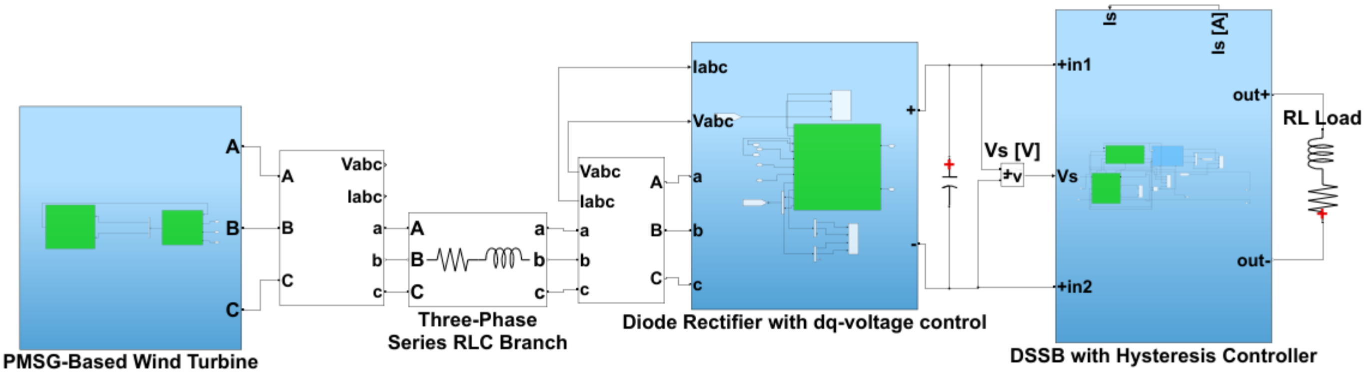

Figure 11. Schematic diagram of the hysteresis current-mode-regulated DSSB regulator along with the PMSG wind turbine and three-phase diode bridge rectifier.

5.1. Control of the DSSB Input Voltage

In conjunction with an additional voltage control loop, the primary objectives of the hysteresis current-mode controller of the DSSB are to control the DC link voltage, $V_s = V_{dc1}$, and the output rectifier current, I_s, which are the input variables of the DSSB regulator. The second objective is to control both the DSSB output current, $I_{o,}$ and the DC link voltage, $V_o = V_{dc2}$, at the DSSB output at the input of the VSI. This allows for the regulation of both the active DC powers generated at the DSSB regulator's input and output [2,22,23].

Therefore, the magnitudes of the PMSG output voltage and current are transformed into dq-coordinates, and the PLL block mentioned in [22–24] provides the PMSG voltage phase and frequency data. In the control stage, these variables are used as measured magnitudes along with the $V_s = V_{dc1}$ voltage.

Consequently, to control the output DC link voltage, V_s, the PMSG direct current (d-axis current) uses the output of this external voltage control loop as a reference. The current in question is, in fact, in phase with the PMSG voltage, accounting for the active power fed into the system. Consequently, if the power demand at the rectifier's output suddenly rises, the DC link voltage, V_s, will drop, and the voltage control will need to raise the reference for the d-axis current, i_d^*, to supply the DSSB with more active power, and raise the DC link voltage level back to its nominal value.

Furthermore, the reference for the q-axis current component, i_q^*, is determined by the desired power factor at the rectifier's input. In case a unity factor of power is needed, the PMSG's reactive power can be zero by setting this reference to zero [22–24].

To determine the transfer function for the DC link voltage at the output of the rectifier circuit, the active power of the system is examined. The following equation illustrates a power transfer that occurs if the losses in the MSC are ignored:

$$P_{gen} = \frac{3}{2} V_{ds}\ I_{ds} = (P_s = V_s\ I_s) + C\ V_{dc1}(dv_{dc1}/dt) \tag{21}$$

where $P_s = V_s\ I_s$ is the DC active power delivered to the DSSB regulator, and $P_C = C\ V_{dc1}(dV_{dc1})/dt$ is the power of the input capacitor of the DSSB regulator, accumulated and delivered interchangeably. After disregarding the power of the DSSB input capacitor, since it is zero during normal operation, the source current's reference value of the DSSB regulator is given as

$$I_s^* = \frac{P_{gen}^*}{1.5\ V_{ds}} \tag{22}$$

Moreover, the current flowing from the DSSB regulator's source, I_s, is related to the d-axis value of the PMSG output current, I_{ds}, through the following transfer function:

$$H_{ii}(s) = \frac{I_s}{I_{ds}} = 1.5\,\frac{V_{ds}}{V_s} \tag{23}$$

Similarly, assuming the plant is schematized in Figures 6 and 11, the control current loop for the stator phase current can be proposed and tuned. Based on Equation (6), one may write

$$G_i(s) = \frac{I_{ds}}{V_{ds}^*} = \frac{1}{R_s + sL_d} = \frac{1}{R_s\ (1 + s\tau_d)} \tag{24}$$

Figure 12 displays the two closed loops, an external voltage loop and an internal current loop, of the voltage control block diagram that are typically used in DC link voltage control loops. To allow tracking of a DC link voltage reference, V_{dc1}^*, the corresponding compensators (k_v(s) and k_{ii}(s)) can also be identical and optimized as PI controllers. If the control employs a zero-pole cancellation scheme [22–24], the transfer function of these PI regulators will be as follows:

$$k_v(s) = k_p\ (1 + \frac{k_i}{s}) \tag{25}$$

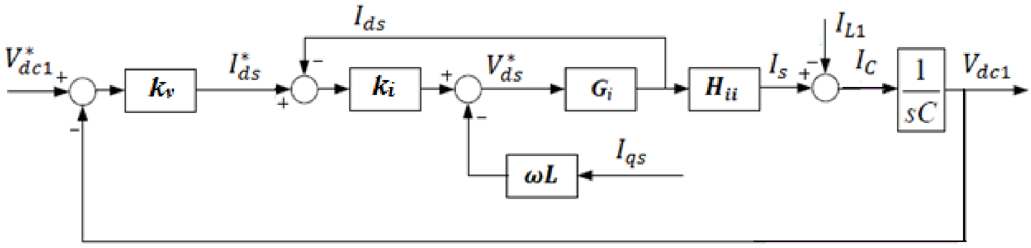

Figure 12. Block diagram of DC link voltage loop control.

While the integral control gain, K_i, is chosen using the trial-and-error method, the proportional control gain is

$$K_p = 2\pi * B_v * C * \frac{3V_{ds}}{2\ V_{dc1}} \tag{26}$$

where B_v is the intended voltage control loop bandwidth. It is important to note that there are numerous potential controllers and various control tuning techniques for each of them.

Additionally, k_{ii}(s) can be a straightforward proportional–integral (PI) compensator to allow tracking of the PMSG stator current Ids' d-axis references. Thus,

$$k_{ii}(s) = \frac{k_p s + k_i}{s} \tag{27}$$

where $k_p = L_d/\tau_d$ and $k_i = \frac{R_s}{\tau_d}$ are proportional and integral control gains, respectively [25].

For a quick current-control response, τ_d needs to be small, but it should also be large enough so that the closed-loop control system's bandwidth, or $1/\tau_d$, is significantly smaller—for instance, ten times—than the DSSB's switching frequency (expressed in rad/s). A range of 0.5–5 ms is usually used to select τ_d, depending on the regulator switching frequency and the needs of a particular application.

After the DC link voltage at the output of the rectifier at the input of the DSSB regulator, $V_{dc1} = V_s$, is regulated and set as shown in Figure 12, it will be utilized as a control parameter for the hysteresis current-mode control of the suggested DSSB regulator.

5.2. Control of the DSSB Input Choke Current

The promoted DSSB circuit and its ramp-hysteresis current-mode control block structure are depicted in Figure 13. A condensed structure of the recommended regulator's hysteresis current-mode controller is presented in Figure 14. When the desired source current, $i_L^* = {i_s}^*$, is compared to the actual source choke current, $i_L = i_1 \cong i_s$, a current error occurs. After comparing the actuating current error to an expected hysteresis window limit (bandwidth), the proper gate pulses for the DSSB regulator active switches are then created with the necessary shifted switching. Both the frequency and the hysteresis window limit (bandwidth) are fixed when using a double-hysteresis current-mode controller [24–26].

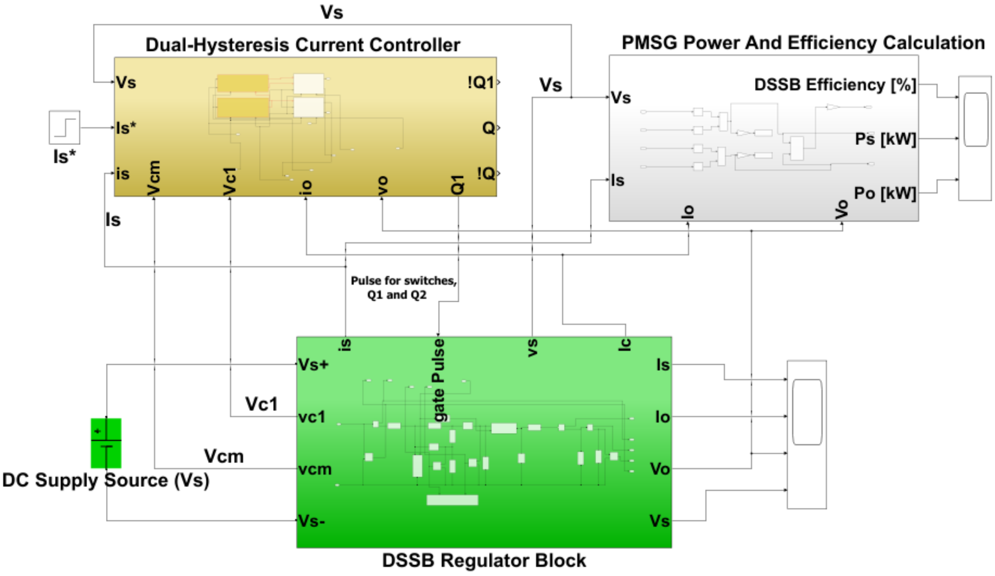

Figure 13. Diagram of the recommended DSSB along with the ramp-hysteresis current-mode control block.

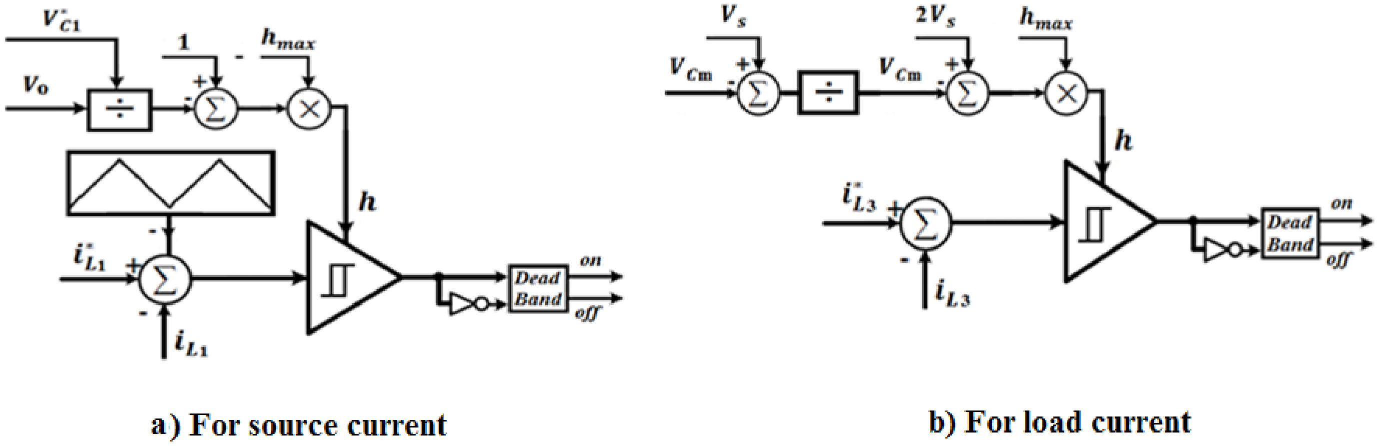

a) For source current

b) For load current

Figure 14. The block structure of a const. frequency hysteresis current-mode controller with fixed window limits.

Regarding the source current hysteresis window limit (bandwidth) determination, the appropriate choke voltage V_{L1}^{*} is represented by the following equation in the off state of the MOS1 switch:

$$V_{L1}^{*} = L_1 \frac{\Delta(i_L^{*} - i_L)}{t_{off}} = \frac{h_s\, L_1}{t_{off}} = V_s - V_{cm} \;\Rightarrow\; t_{off} = \frac{h_s\, L_1}{V_s - V_{cm}} \tag{28}$$

The hysteresis window limit, h, is utilized to control the DSSB input choke current. The following formula yields the desired choke voltage V_{L1}^{*} when the main switch, MOS1, is in the on state:

$$V_{L1}^{*} = L_1 \frac{\Delta(i_L^{*} - i_L)}{t_{on}} = L_1 \frac{h_s}{t_{on}} = V_s \Rightarrow t_{on} = \frac{h_s\, L_1}{V_s} \tag{29}$$

Thus, bringing together Equations (28) and (29) leads to

$$h_s(t) = h_{max} \frac{(V_s - V_{cm})}{(2\, V_s - V_{cm})} \tag{30}$$

Equation (30) represents the hysteresis window limit, $h_s(t)$, for the source current, i_L. Concerning the hysteresis window limit, $h_o(t)$, for the load current, i_o, one may write the following expressions:

$$V_{L3}^{*} = L_3 \frac{\Delta\left(i_{L3}^{*} - i_{L3}\right)}{t_{off}} = \frac{h_o\, L_3}{t_{on}} = V_{C1} - V_o \;\Rightarrow\; t_{on} = \frac{h_o\, L_3}{V_{C1} - V_o} \tag{31}$$

where V_{L3}^{*} is the inductive voltage of output load choke, L_3, that is obtained during the on state of the MOS2 switch [24–26]. The DSSB load choke current is represented by $i_{L3} \approx\; i_o$, while the reference load choke current is represented by $i_{L3}^{*} = i_o^{*}$. The desired choke voltage V_{L3}^{*} will be ascertained when the switch is in the off state and is as follows:

$$V_{L3}^{*} = L_3 \frac{\Delta\left(i_{L3}^{*} - i_{L3}\right)}{t_{off}} = L_3 \frac{h}{t_{off}} = V_o \Rightarrow t_{off} = \frac{h_o\, L_3}{V_o} \tag{32}$$

Consequently, the subsequent equation for the hysteresis window limit of the load current is calculated through the combination of Equations (31) and (32):

$$h_o(t) = h_{max} \frac{(V_{C1} - V_o)}{V_{C1}} = h_{max} \left(1 - \frac{V_o}{V_{C1}}\right) \tag{33}$$

In both scenarios of Equations (30) and (33), the maximum hysteresis bandwidth, $h_{max} = \frac{V_s}{f\, L_1}$, is closely linked to the supply voltage, V_s, and negatively correlated with the regulator's switching frequency [26].

By monitoring the average value in a succession of inputs, the average-value block in Figure 15 is utilized to calculate the overall average value of the output voltage, V_o, and capacitor voltages, V_{C1} and V_{cm}, across a range of inputs over an extended period of time [26].

Figure 16 shows the regulation method used to produce the necessary cycle, D1, for MOS1 based on the mathematical study, while Figure 17 shows the approach used to produce the necessary reference cycle, D2, for MOS2 [26].

The modulation technique for MOS1, which generates gate pulses after determining the necessary cycle, D1, is depicted in Figure 18. After determining the reference cycle, D2, Figure 19 illustrates the switching method for producing the gate pulses for the suggested regulator switch MOS2. Consequently, these two PWM signal generators are used to produce two distinct activating signals, one for MOS1 and the other for MOS2, separated by a time shift.

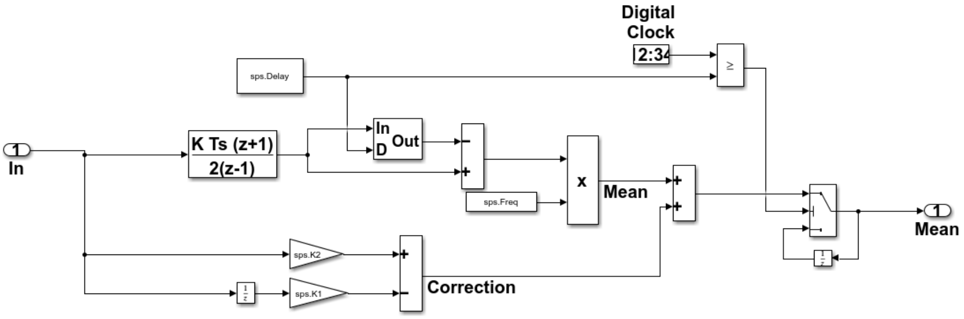

Figure 15. Mean-value block for computing the total average value of capacitor voltages using MATLAB.

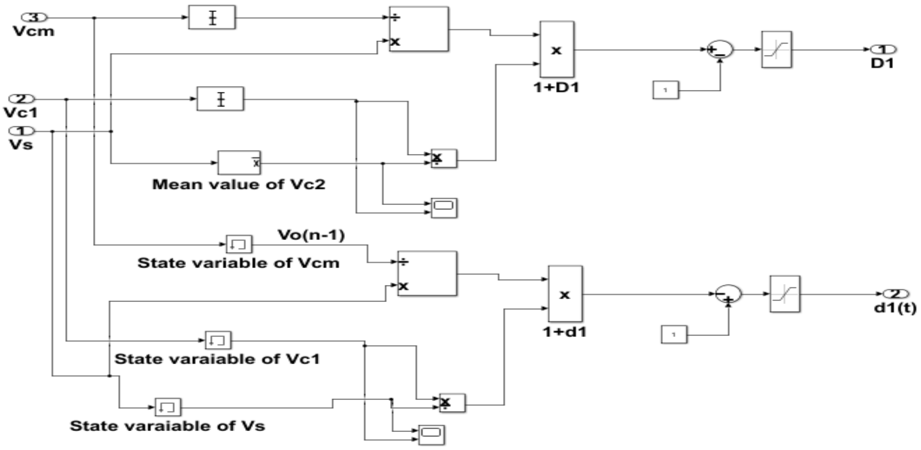

Figure 16. Control scheme to produce reference cycle for MOS1 switch.

To test the proposed double-hysteresis control algorithm under variable operating conditions, the next step of the simulation will be to determine how well the regulator performance performs in response to variations in wind speed, with a starting point of 12 m/s and a final increase to 16 m/s and 20 m/s, along with a constant source current.

Figure 20 shows the input and output currents, voltages, and input/output powers in addition to the effectiveness of the DSSB regulator with the recommended double-hysteresis current controller under a variable wind speed (12 m/s, 16 m/s, 20 m/s). Along with the mechanical torque (τ_m), electromagnetic torque (τ_e), and wind turbine speed (ω_r), it also shows the active power (P_{gen}) and reactive power (Q_{gen}) of the PMSG.

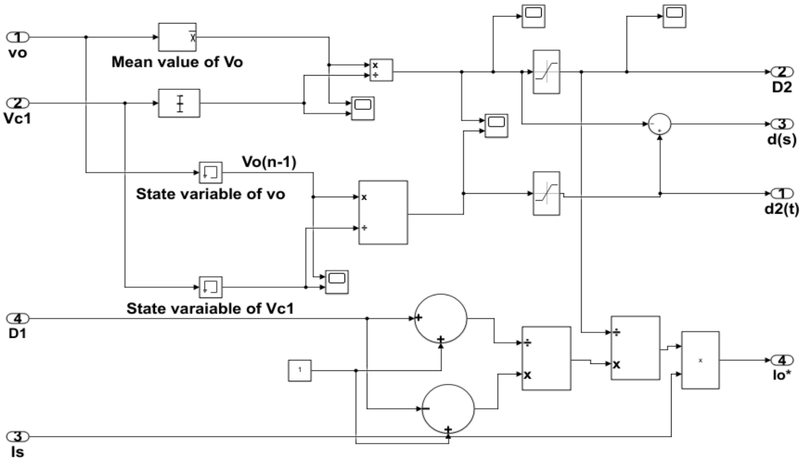

Figure 17. Control scheme to produce reference cycle for MOS2 switch.

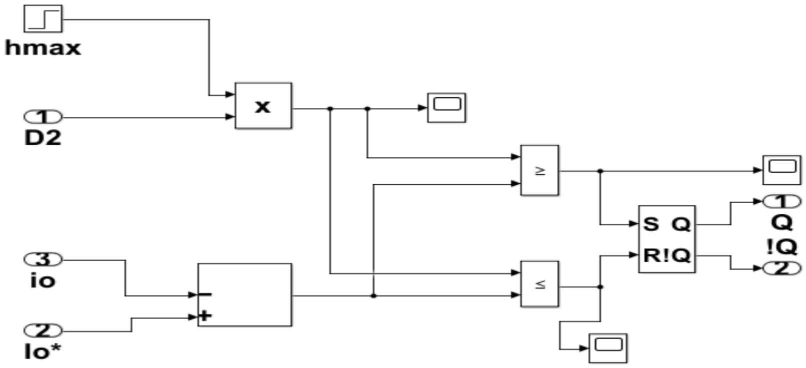

Figure 18. MATLAB/Simulink-built constant frequency of established bandwidth of double-hysteresis current-mode controller framework for MOS1.

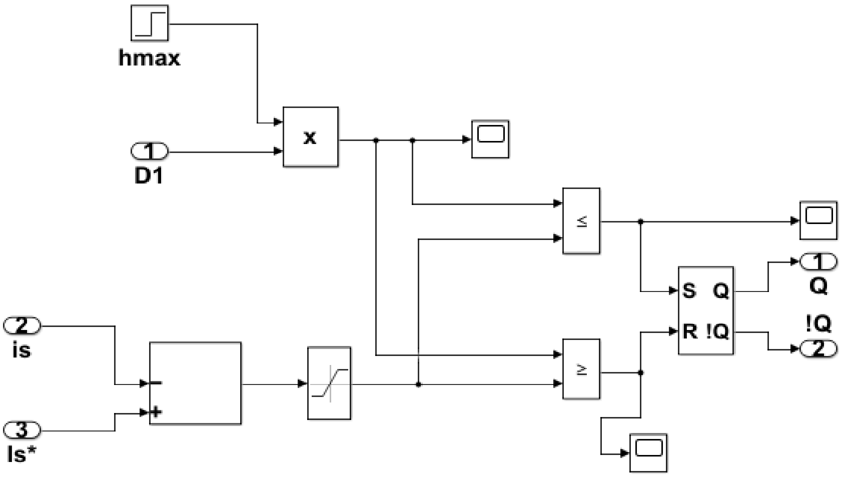

Figure 19. MATLAB/Simulink-built constant frequency of fixed bandwidth of double-hysteresis current-mode controller framework for MOS2.

The load resistance, switching frequency, and source current of the regulator are all fixed at 10 kHz, 40 A, and 10 kHz, respectively [26–30].

Along with its high efficiency, the regulator also exhibits improved performance in terms of standardized ripple in voltage and current, as well as a quick response with short rising and settling times.

The short rise time of 0.15 s and low harmonic content of the system, as illustrated in Figure 20, best describe its capacity to react to abrupt variations in wind speed. Additionally, this figure illustrates how systematic variations in the DSSB input and output powers yield the same regulator efficiency values as when the source current and wind speed are constant. The PMSG reactive power, Q_{gen}, the transient in DSSB input/output powers, P_s and P_o, and the PMSG active power, P_{gen}, are more noticeable. The wind turbine operates continuously within the permitted power range. Furthermore, the fact that the regulator keeps the source current constant even though the output voltage and output current vary between 420 V, 500 V, and 580 V and 8.4 A, 10 A, and 11.4 A indicates that the conversion process is operating as intended. This suggests that the recommended hysteresis current-mode controllers are compatible with the regulator's conversion mechanism [22,30].

Additionally, Figures 20c and 21 show the effective performance of the regulator's suggested control algorithm by analyzing the PMSG rotor speed and electromagnetic torque waveforms, the turbine's mechanical torque (Figure 20), and the PMSG dq-axis currents and voltages (Figure 21) in response to step changes in wind speed. The PMSG electromagnetic torque increases to the rated value as soon as the generator speed increases. On the other hand, the generator accelerates, and the rotor speed rises due to the difference between the generator torque (τ_e) and the turbine drive torque (τ_m). Moreover, while the PMSG rotor speed varies in steps from 134 rad/s to 188 rad/s to 240 m/s, the turbine mechanical torque and PMSG electromagnetic torque remain constant when the wind speed is changed from 12 m/s to 16 m/s and then to 20 m/s.

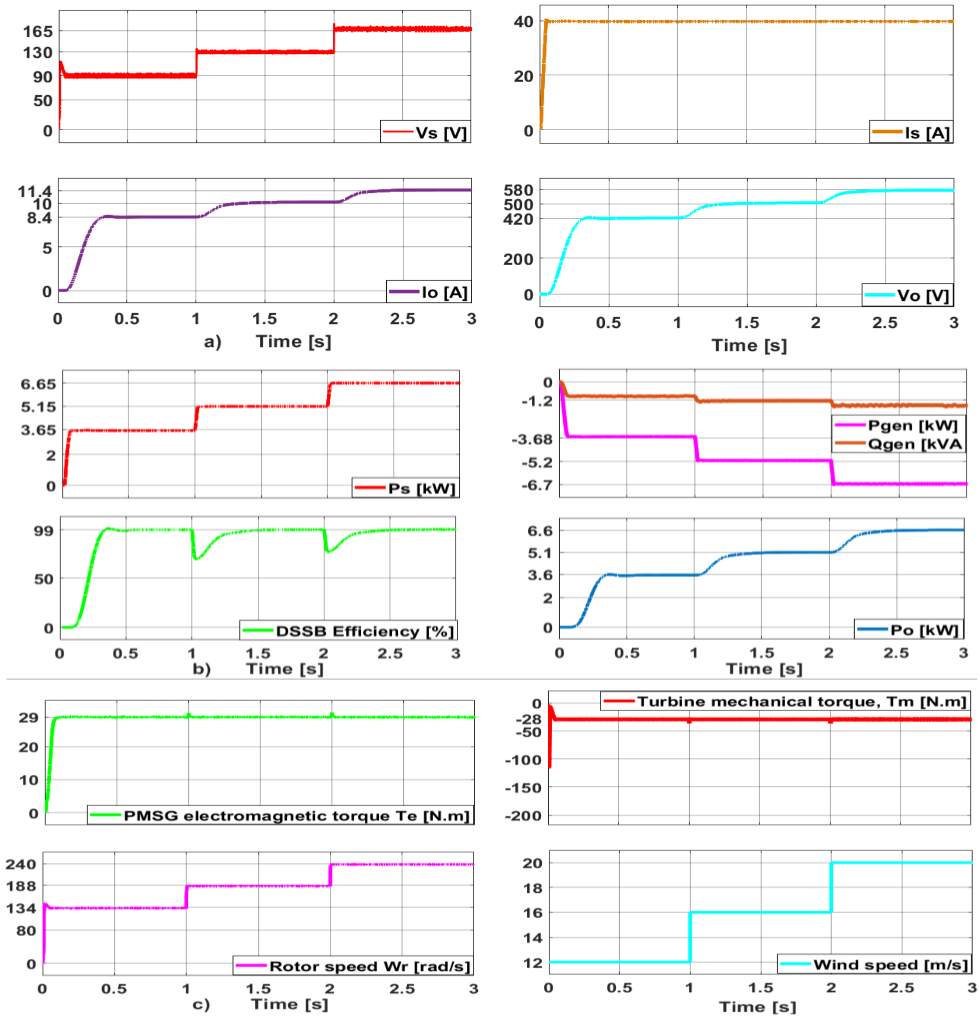

Figure 20. Results of MATLAB simulation of DSSB-based hysteresis controller with constant source current (40 A) and step changes in wind speed (12 m/s, 16 m/s, 20 m/s): (**a**) DSSB output/input voltages and currents. (**b**) DSSB output/input powers with efficiency and PMSG output active and reactive powers (P_{gen} & Q_{gen}). (**c**) Torques and rotor speed. Target frequency = 10 kHz.

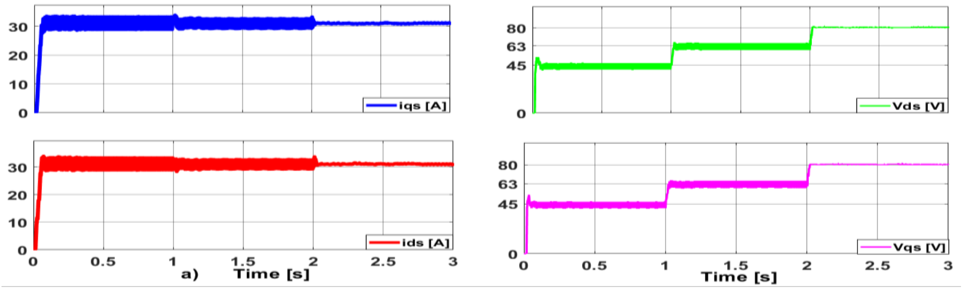

Figure 21. *Cont.*

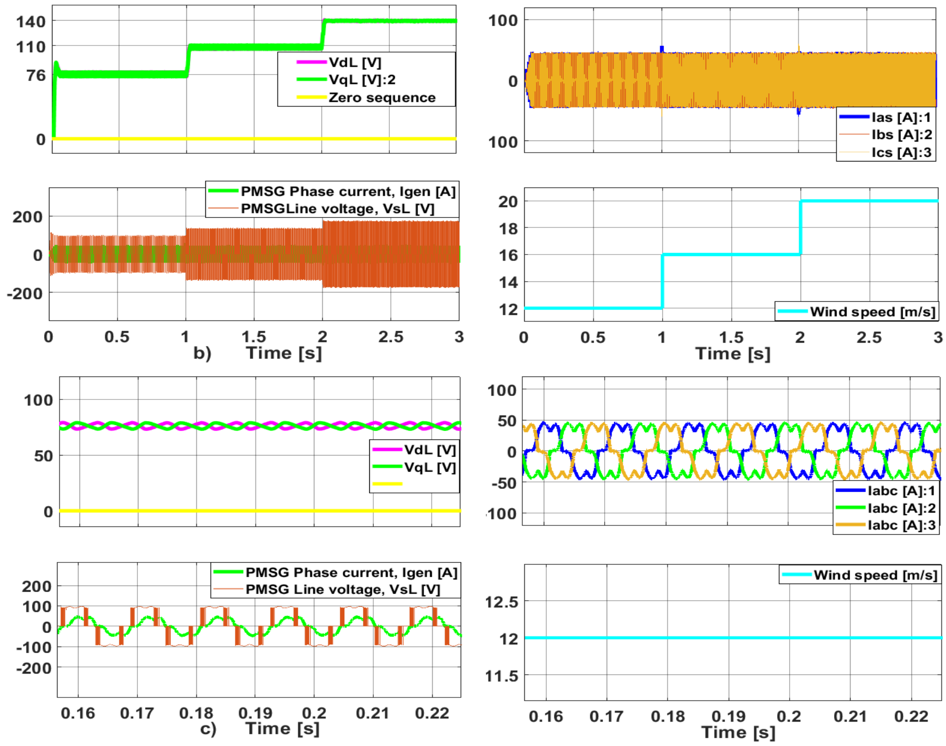

Figure 21. Results of MATLAB simulation of DSSB-based hysteresis controller with constant source current (40 A) and variable wind speed (12 m/s, 16 m/s, 20 m/s): (**a**) dq-axis phase voltages (V_{ds}, V_{qs}) and dq-axis phase current (I_{ds}, I_{qs}) of PMSG. (**b**) PMSG stator currents (I_{as}, I_{bs}, I_{cs}) and PMSG dq-axis line voltages (V_{dL}, V_{qL}). (**c**) Snapshot of PMSG stator currents (I_{as}, I_{bs}, I_{cs}) and PMSG dq-axis line voltages (V_{dL}, V_{qL}) at a wind speed of 12 m/s. Target switching frequency = 10 kHz.

6. Front-Loading Inverter Control at the Grid/Load Side

To connect the wind turbine generators to the grid, a front-loading inverter (grid-side inverter), VSI, is used. It is responsible for regulating the quantity of reactive and active power that enters the system. There are multiple control strategies for the grid-side VSI. All of them have the same objectives: regulation of the voltage at the DC-link, controlling the quantity of reactive and active power fed into the grid, and synchronizing the grid to ensure the system runs consistently [23–30].

6.1. VSI Field-Oriented Control-Based Decoupled Current Controller in dq Reference Frame

The field-oriented control arrangement for the front-loading VSI is depicted in Figure 22. The control scheme consists of two loops. The reactive power and the DC link voltage are managed by the exterior loop, while the grid current is managed by the interior loop. By adjusting the amount of active and reactive power supplied to the grid, the exterior loops control the system's power flow [28–32]. All the grid-side inverter variables are DC components in a steady state because of the employment of the field-oriented regulation scheme within the synchronous reference frame. Using phase-balanced sinusoidal waveforms for the grid voltages v_{ag}, v_{bg}, and v_{cg}, the grid voltage angle can be computed as follows [26–32]:

$$\begin{aligned} v_{ag} &= R_g\, i_{ag} + L_g \frac{di_{ag}}{dt} + v_{ao} \\ v_{bg} &= R_g\, i_{bg} + L_g \frac{di_{bg}}{dt} + v_{bo} \\ v_{cg} &= R_g\, i_{ag} + L_g \frac{di_{cg}}{dt} + v_{co} \end{aligned} \tag{34}$$

where the line inductance and resistance are denoted by L_g and R_g, respectively. At the inverter output, the voltages are represented by v_{ao}, v_{bo}, v_{co}. The line currents are i_{ag}, i_{bg}, and i_{cg}. Since the line resistance R_g is so tiny, this analysis typically ignores it. Thus, one may write the following for the phasor current and phasor voltage:

$$v_{abcg} = L_g \frac{di_g}{dt} + v_{abco} \tag{35}$$

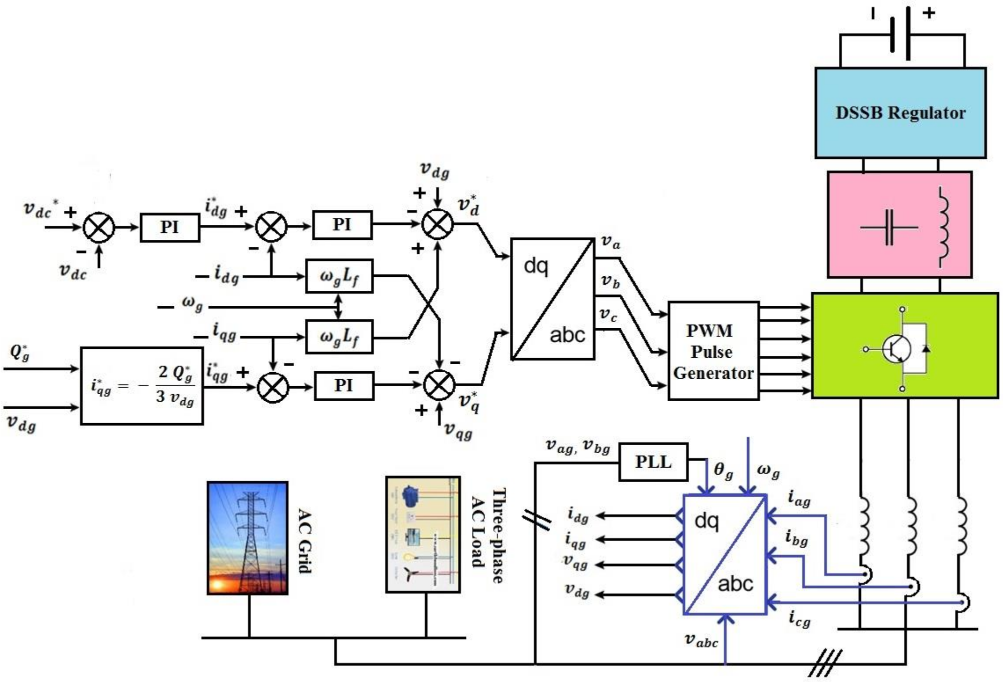

Figure 22. Front-loading inverter in grid-connected mode with DSSB, a diode rectifier, and a DC voltage source, E.

The dq frame alignment at $t = 0$ determines the transformation from abc to dq. The position of the rotating frame is indicated by $\theta_g = \omega_g t$ concerning phase (a), where ω_g is the dq frame rotation speed or the angular frequency of the grid. The following relations are obtained when the phase a-axis and the rotating frame are aligned:

$$\overline{v_g} \;=\; v_{dg} + jv_{qg} = \left(v_{\alpha g} + jv_{\beta g}\right).\, e^{-j\omega_g t} = \frac{2}{3}\left(v_{ag} + v_{bg}.e^{-j\frac{2\pi}{3}} + v_{cg}e^{j\frac{2\pi}{3}}\right)e^{-j\omega_g t} \tag{36}$$

Using the dq transformation in the rotating reference frame, one may obtain the following voltage equations [26–32]:

$$\begin{aligned} v_{dg} &= v_{do} \;-L_g \tfrac{di_{dg}}{dt} + \omega_g\, L_g\, i_{qg} \\ v_{qg} &= v_{qo} \;+L_g \tfrac{di_{qg}}{dt} - \omega_g\, L_g\, i_{dg} \end{aligned} \tag{37}$$

The dq transformation may also be used to obtain the active and reactive powers as follows:

$$\begin{aligned} P_g &= \tfrac{3}{2}\,(v_{dg}\, i_{dg} + v_{qg}\, i_{qg}) \\ Q_g &= \tfrac{3}{2}\left(v_{dg}\, i_{qg} + v_{qg}\, i_{dg}\right) \end{aligned} \tag{38}$$

Maximizing the efficiency at the output is achieved by regulating $i_{qg} = 0$, which ensures minimum reactive power for a given load (grid). The previously mentioned formulas show that active/reactive power can be controlled by adjusting the dq-axis currents, respectively [29–34]. One can obtain the dq-axis current references i_{qg}^* and i_{dg}^* as follows:

$$\begin{aligned} i_{qg}^* &= \frac{2Q_g^*}{3v_{dg}} \\ i_{dg}^* &= \frac{2P_g^*}{3v_{dg}} \end{aligned} \tag{39}$$

where Q_g^* is the reference value of the reactive power; it has a positive value for lagging power-factor loads and a negative value for leading ones. It equals zero for unity power-factor loads.

On the AC side of the inverter, the active power is equal to the DC power on the DC side, if the losses in the inverter are ignored. As such,

$$P_g = \frac{3}{2}\left(v_{dg}\, i_{dg}\right) = v_{dc}\, i_{dc} \tag{40}$$

Depending on the inverter's operating state, the reference value for the d-axis current is produced by the PI controller for the direct current (dc) link voltage, i_{qg}^*. The inverter's DC link voltage v_{dc} is controlled by the proposed regulator DSSB to a given value v_{dc}^* based on the required value at the output of the inverter, which is given as [31–36]

$$v_{dc}^* = 2\sqrt{2}\,\frac{V_{ag}}{m} = \frac{2\sqrt{2}}{\sqrt{3}}\,\frac{V_{abg}}{m} \tag{41}$$

In this case, V_{ag} represents the mean square value of either the load (grid) phase voltage or the inverter output voltage, and V_{abg} stands for the mean square value of either the load line voltage or the inverter line voltage. The symbol m is used for the modulation index of the inverter ($0 < m \ \leq 1$).

6.2. Determination of the Decoupled Current PI Controllers

Equation (37) shows how the d-axis and q-axis current variables, and the derivative of the dq-axis currents are related. Any adjustments made to the q-axis variables will affect the d-axis current, and vice versa. Consequently, as illustrated in Figure 22, two decoupled current PI controllers are utilized to resolve this issue. One can obtain the output of the decoupled current controllers as follows [34,36]:

$$\begin{aligned} v_{do} &= -\left(k_p + \tfrac{k_i}{s}\right)\left(i_{dg}^* - i_{dg}\right) + \omega_g\, L_g\, i_{qg} + v_{dg} \\ v_{qo} &= -\left(k_p + \tfrac{k_i}{s}\right)\left(i_{qg}^* - i_{qg}\right) + \omega_g\, L_g\, i_{qg} + v_{qg} \end{aligned} \tag{42}$$

From Equation (42), for the dq-axis currents, one may obtain the following:

$$\begin{aligned} \tfrac{di_{dg}}{dt} &= \tfrac{1}{L_g}\left(k_p + \tfrac{k_i}{s}\right)\left(i_{dg}^* - i_{dg}\right) \\ \tfrac{di_{qg}}{dt} &= \tfrac{1}{L_g}\left(k_p + \tfrac{k_i}{s}\right)\left(i_{qg}^* - i_{qg}\right) \end{aligned} \tag{43}$$

Equations (42) and (43) demonstrate the decoupling of the d-axis and q-axis currents, where the PI controller design is now simpler and has better performance [35–37].

When the inverter is operating in stand-alone mode, its job is to control the frequency and voltage of the inverter output because there is no grid. Within the revolving reference frame, a field-oriented control structure with split-current controllers is employed. The frequency of the inverter output voltage (load voltage) and current, $\omega = 2\pi f$, is the value that the controller sets for the angular speed of the rotating reference frame. The voltage and current controllers are in the outer and inner loops, respectively. To bring the d-axis voltage to its assessed value, the voltage regulator (PI) modifies the output voltage at varying wind speeds and load transients. The dq-axis current components are managed by the current PI controllers in the inner control loop. To compensate for the cross-coupling caused by the output filter inductance, the compensation terms are added to the decoupled current controllers.

6.3. Effect of LCL Filter Cables between the Grid and the Inverter

The grid-connected-mode performance of the grid-side inverter controllers is displayed in Figure 22. If the grid is connected directly to the inverter without an LCL filter in between, it may experience overcurrent and overvoltage in the grid phase and line voltages. This could lead to undesirable harmonic reactive and active power components in the system.

To enhance the stability of the voltage/current control and prevent resonance effects and harmonic generation into the grid, an LCL filter with a passive resistive damping element will be incorporated into the system. Thus, by using a highly inductive filter with specific shunt capacitance values between the lines—where both reactants have a sufficient damping effect—it is possible to reduce the current harmonics surrounding the switching frequency, and the power fluctuation and efficiency. A T-model of a two-port circuit is used in Figure 23 to represent the filter cables that are used to improve the performance of the grid-side inverter. To take further advantage of this method's benefits, there are four other possible connections, as explained in [30–38].

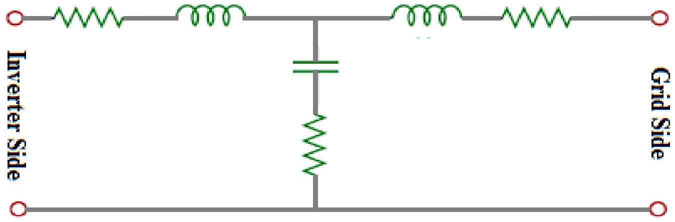

Figure 23. A per-phase T-model of a two-port cable connected between the grid and the VSI.

In Figure 22, the simulation is illustrated after removing the DSSB regulator and considering the following parameters of the grid and the LCL filter components:

Depicting the result of the simulation, Figure 24a shows the phase voltage, V_f, across the LCL filter with the grid, and the line voltage, V_{fL}, between two phases of the LCL filters with the grid. It also shows the VSI phase current and phase voltages, V_a and I_a, that are injected into the grid via the LCL filters. Figure 24b displays the line voltage V_{gL} between two grid phases as well as the grid phase currents and voltages, V_{gabc} and I_{gabc}, with the VSI DC supply voltage, V_{dc}. The simulation is performed using the parameters from Table 2.

Table 2. Parameters of the grid with LCL Kalman filter circuit between the grid and the inverter.

Parameter	Real Value
DC link voltage	6000 V–12,000 V
Grid phase-to-phase voltage	6000 V
Grid internal inductance	16.58 mH
Grid internal resistance	0.8929 Ω
Parameters of the LCL Kalman filter on the inverter side	1 mH and 0.5 Ω
Parameters of the LCL Kalman filter on the grid side	1 mH and 0.5 Ω
Filter capacitance	5 mF
Filter resistance	0.5 Ω
Grid frequency	50 Hz
Inverter frequency	10 kHz

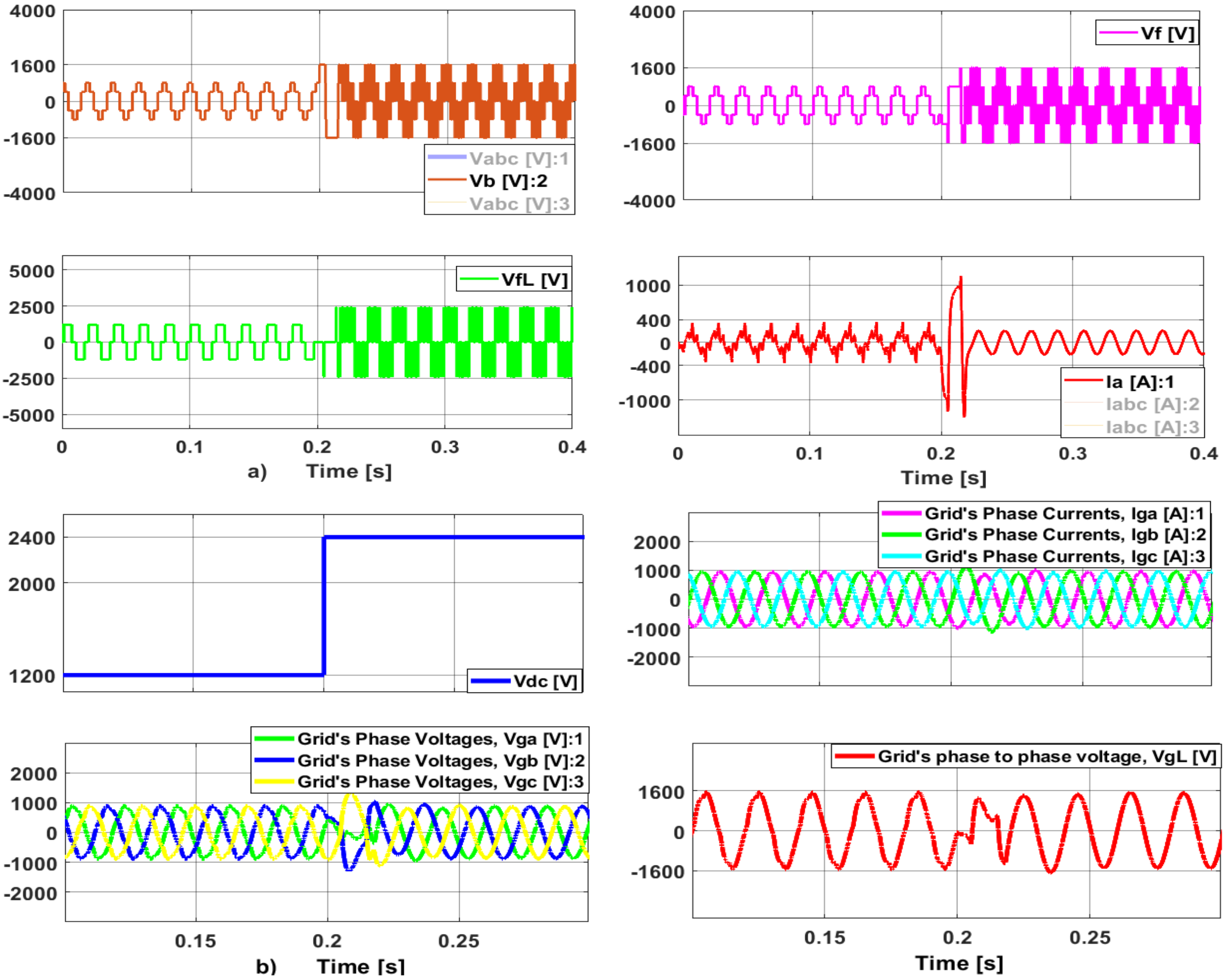

Figure 24. Performance of the grid-side inverter that is connected to the grid through LCL Kalman filters, and is subjected to a stepwise variation in the constant DC source of between 1200 and 2400 volts. The PMSG, DSSB regulator, and wind turbine are removed. (**a**) The phase voltage, $V_f = V_b$, across the LCL filter with the grid, and the line voltage, V_{fL}, across two phases of the LCL filters with the grid, in addition to the phase current flowing through these filters. (**b**) the line voltage (V_{gL}) between two grid phases, as well as the grid phase currents and voltages (Vgabc and Igabc), with the VSI DC supply voltage (V_{dc}).

Figure 25a displays the active and reactive powers (Q_c and P_c) extracted by the shunt resistive–capacitive element of the LCL Kalman filters, as well as the active and reactive powers (P_g and Q_g) supplied by the grid. Furthermore, Figure 25a displays the active and reactive powers of the LCL Kalman filter series elements, P_f and Q_f, as well as the DC power supplied from the VSI DC source to the remaining portion of the system under consideration, P_{dc}.

The observed values of the grid's active and reactive powers are negative, indicating that the remaining components of the system under consideration are receiving power from the grid in both forms. The dq-axis voltages and currents of the grid are displayed in Figure 25b. In comparison to the q-axis voltage and d-axis current, it is observed that the d-axis voltage and q-axis current have smaller values. This illustrates how the active and reactive power may be controlled under various DC-link VSI voltages by using the q-axis voltage and the d-axis current, respectively.

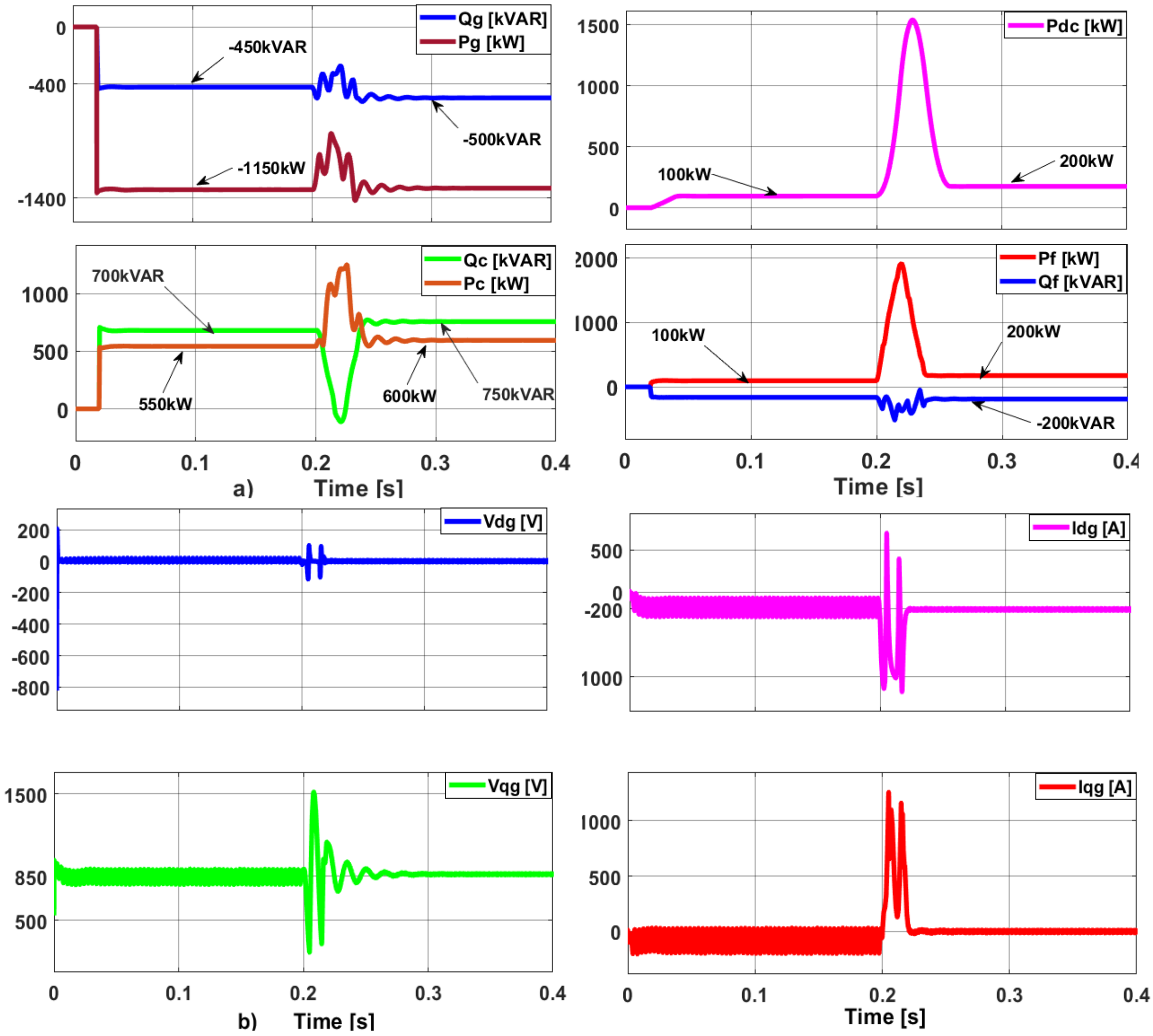

Figure 25. Performance and power capacity of the grid with the VSI after the wind turbine, PMSG, and DSSB were removed, along with a stepwise variation in the DC source of between 1200 and 2400 volts: (**a**) Active and reactive powers on the inverter side (P_f and $Q_{f,}$), the grid side (P_g, and Q_g), and the LCL filter side (P_c and Q_c) (**b**) dq-axes currents and voltages of the grid.

7. Simulation Results

In this paper, the perturbation and observation of the MPPT method for a PMSG are investigated. The PMSG is driven by a wind turbine and supplies an AC load (*RL*, or AC grid) via a hysteresis current-mode-regulated DSSB regulator, and a dq-current vector-controlled triple-phase voltage source, VSI.

Decoupled dq-axis current controllers are used to implement the field-oriented control of the front-loading VSI in Simulink/MATLAB. Sample times of 20 µs are employed by the inner and outer current-control loops, respectively.

The specification parameters listed in Table 3 are used for the DSSB regulator. The specification parameters for the wind turbines and PMSG are shown in Table 4.

Table 3. Design specifications of DSSB.

Parameter	Symbol	Real Value
Input choke	L_1	100 mH
Shunt choke	L_2	10 mH
Output choke	L_3	670 μH
Smoothing capacitor	C_s	470 μF
Shunt capacitor	C_m	470 μF
Shunt capacitor	C_1	470 μF
Output capacitor	C_o	5 mF
Load resistance	R	10 Ω
Switching frequency	f	10 kHz

Table 4. Wind turbine and PMSG parameters.

Wind Turbine Parameters	
Assessed power	12.3 kW
Assessed wind speed	12 m/s
Cut-in speed	4 m/s
Cut-out speed	24 m/s
Air density	1.225 kg/m^3
Power factor	0.85
Turbine rotor radius	1.3 m
PMSG Parameters	
Assessed power	1.1 MW
Assessed voltage	3.3 KV
Number of pole pairs	3
Stator resistive element, R_s	0.0485 Ω
d-component of synchronous inductance	0.395×10^3 H
q-component of synchronous inductance	0.395×10^3 H
Rotor flux, λ_f	0.1194 Web
Rotor flux position when theta = 0	90° behind phase A axis
Power factor	0.85

7.1. WECS with PMSG, DSSB, and VSI Supplying RL ($R = 20\ \Omega, L = 10$ mH) through LCL Filters

Using MATLAB-Simulink, an investigation of the chosen case study of the suggested WECS system with DSSB, VSI, and a highly inductive AC load is carried out. The size of the simulation step is set to 20 s. The observer and control sample time and controllers are updated every 20×10^6, with a typical PWM 10 kHz for a dq-current-control cycle for the VSI. Other system parts are simulated using a hysteresis current-mode controller. In real-time implementations, the wind speed estimate and the rotor speed management updates may be much longer.

The PI current controller parameters for the grid-side inverter are $k_p = 5$ and $k_i = 5000$. The PLL phase-locked loop's PI controller parameters for the load/grid-side inverter to estimate the frequency of the AC load (grid) are $k_p = 10$ and $k_i = 5000$.

The primary goal of the hysteresis current-mode MPPT-regulated DSSB regulator controller is to limit the maximum power absorbed for the wind turbine's safe operation and to extract the optimal power under changing wind speeds. The WECS system, including the turbine, PMSG, DSSB, and front-loading inverter, which are shown in Figure 1, is now simulated with the load treated as an RL-load for the specified parameters mentioned in Table 5.

Table 5. Simulation parameters of AC RL.

Parameter	Symbol	Real Value
Nominal phase-to-phase voltage	V_{gL}	680 V
Active power	P_g	10 kW
Inductive reactive power	Q_g	100 VAR

The simulation is carried out for the boosting (enhancing) regime of the DSSB regulator, which means that $V_s < V_o$. The system waveforms under consideration are shown in Figure 26a–c, where the wind speed varies in a stepwise manner from 10 m/s to 20 m/s in 4 s. While Figure 26a shows the currents and voltages of the load, Figure 26b depicts a shorter time interval for the inverter line and phase voltage with the load phase current when the wind speed is 20 m/s. From Figure 26c, it is seen that the load dq-axis currents and voltages follow their references quite well under variable wind speeds (10 m/s and 20 m/s). Ideal values and improved harmonic distortion can be seen in the dq-axis currents and voltage ripples injected into the load via the VSI. It is also clear from Figure 26c how the active power and the reactive power of the load are related to the load's d-axis current and q-axis current, respectively.

Figure 27a displays the active and reactive powers of the shunt impedance of the LCL filter (P_c and Q_c), the output powers of the VSI (P_f and Q_f), the load reactive power (Q_g), and the active power (P_g), as well as the generator output powers (P_{gen} and Q_{gen}). It is evident how the generator can extract optimal power from the turbine with wind speed variations. The corresponding WECS component is either supplying or absorbing power, as indicated by the positive or negative active or reactive power. However, the DSSB regulator's DC power (P_s or P_o) is always positive, regardless of whether it is sending P_o to the VSI or receiving P_s from the rectifier.

Moreover, the impact of the hysteresis current-mode controller as a response to the step-changing wind speed profile on the performance of the proposed DSSB regulator is depicted in Figure 27b. Additionally, the response of the WECS-rated speed and torque along with the turbine mechanical torque to the wind speed variation is depicted in Figure 27c.

Based on the hysteresis control, the source current, I_s, is set to 40 A. However, the DSSB input/output voltages and current, V_s, V_o, and I_o, vary following the applied DSSB conversion ratio and variations in the wind speed profile.

To monitor the performance of the WECS wind power system under a sudden electrical fault, a wind speed of zero that may occur at the turbine side is considered. Thereby, wind speed variation from 10 m/s to 0 m/s at 2 s, and then to 20 m/s right after 0.5 s, is taken into consideration. As shown in Figure 28a, the PMSG output line voltage (V_{sL}) drops instantly to zero when the fault occurs. Meanwhile, because of this wind speed collapse fault, the PMSG is unable to supply power to the DSSB and subsequently to the load.

Nonetheless, due to the influence of the DSSB energy storage elements with the hysteresis current-mode control that keep the DSSB's source current virtually constant at 40 A, the variation in the power supplied to the load is negligible. This indicates that the load side's active power is still kept at a level that is nearly identical to its previous value before the fault. The power difference between the generator side and the load side is stored in the shunt capacitor, causing the decrease in the DC link voltage ($\mathrm{V_o}$) of the VSI to be negligible.

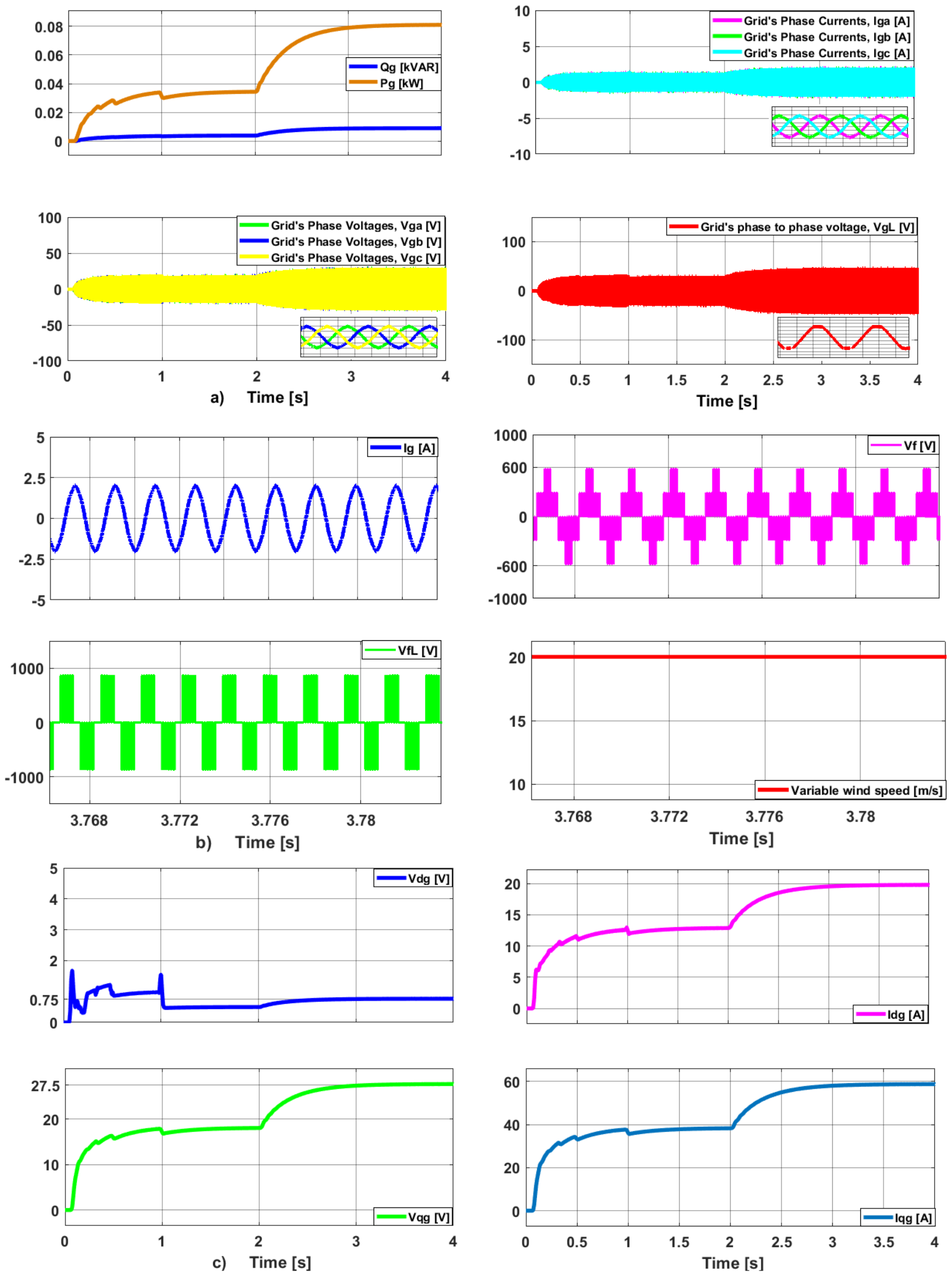

Figure 26. Waveforms of WECS variables as responses to the step change in the wind speed profile (10 m/s and 20 m/s): (**a**) complete waveform: load's phase currents (I_{ga}, I_{gb}, I_{gc}), phase voltages (V_{ag}, V_{bg}, V_{cg}), line voltage (V_{gL}), and active and reactive powers (P_g and Q_g); (**b**) a condensed waveform of the line and phase voltages of VSI together with the wind speed and load phase current; (**c**) load dq-axis currents and dq-axis voltages.

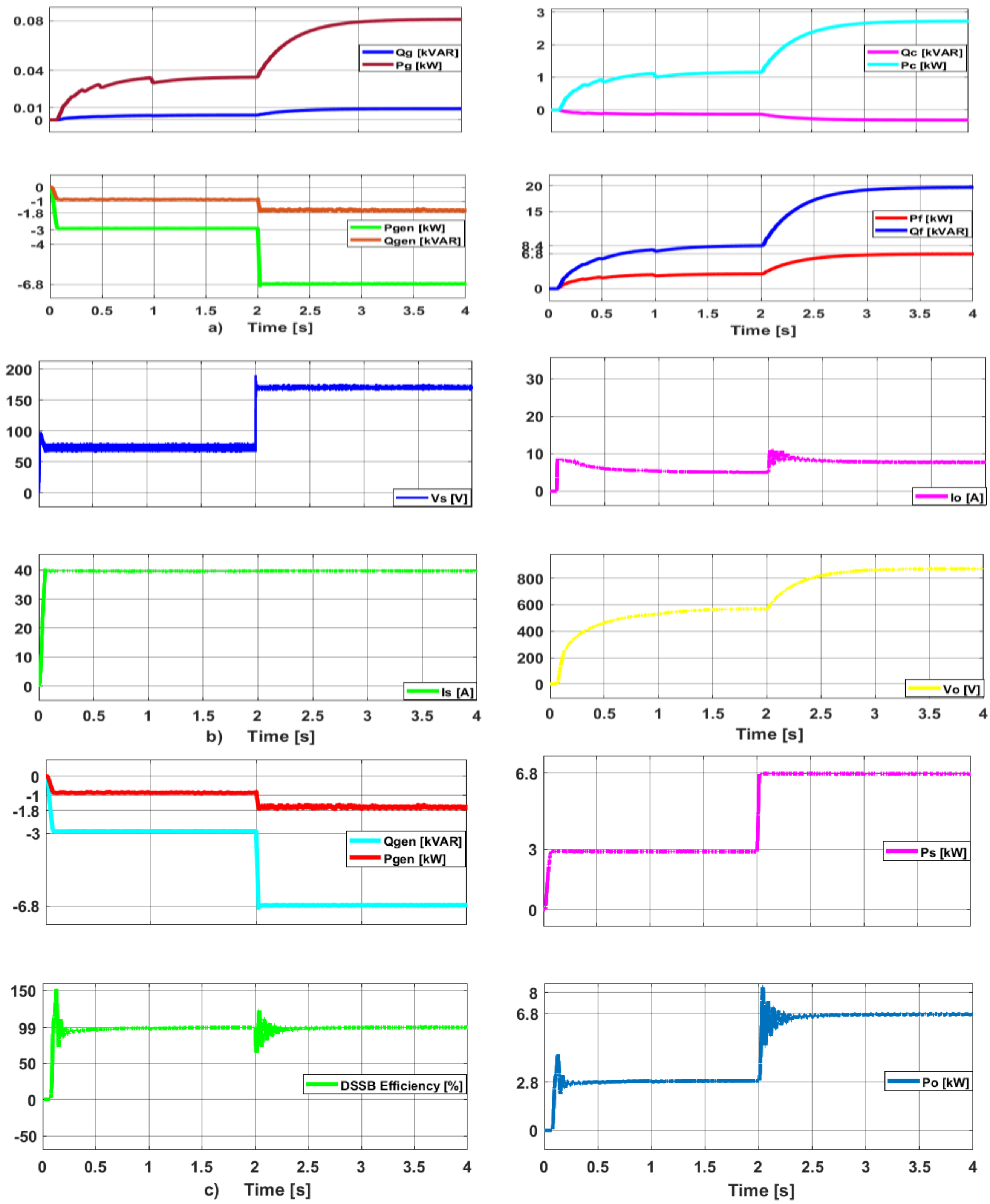

Figure 27. Simulation of WECS variables: (**a**) Active and reactive power of all main WECS system components (AC load, PMSG, DSSB, VSI). (**b**) DSSB output/input currents and voltages as the wind speed changes from 10 m/s to 20 m/s. (**c**) DSSB output and input powers, P_s and P_o, and efficiency with PMSG's active and reactive powers.

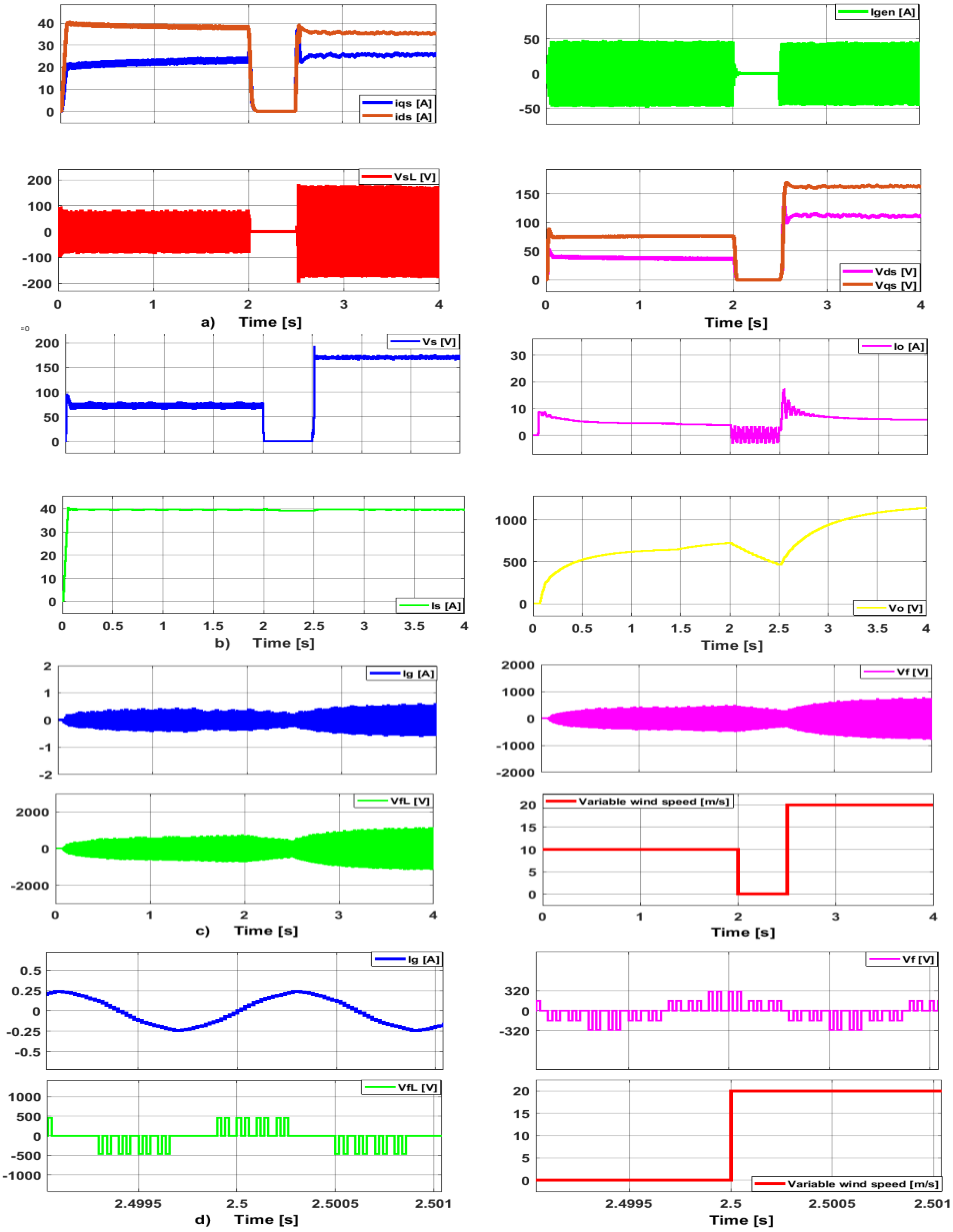

Figure 28. The WECS wind power system's performance in the event of a zero-wind-speed fault: (**a**) PMSG currents and voltages; (**b**) DSSB currents and voltages; (**c**) load-side currents and voltages with wind speed; (**d**) a snapshot of the load-side currents and voltages with wind speed around the fault point.

7.2. WECS with PMSG, DSSB, and VSI Supplying Triple-Phase AC Grid through LCL Filters

The WECS system in Figure 22 is now investigated with an AC grid, whose parameters are listed in Table 6. The field-oriented regulated front-loading inverter (VSI) with a hysteresis current-mode MPPT-regulated DSSB regulator is implemented to reach the maximum power extraction of the WECS system. The MATLAB/Sim Power Systems wind turbine model is used in this work. Again, the PMSG and turbine data used for the simulation are listed in Tables 3 and 4. The torque and speed control loops have sample times of 20 µs and/or 50 µs, respectively. The wind turbine model takes the step-varying wind speed as the input and produces torque as an output. The grid-side inverter's PI current controller settings are the same as previously stated.

Table 6. Grid specification parameters.

Parameter	Real Value
Phase-to-phase grid voltage	680 V
Grid frequency	50 Hz
Grid source inductance	16.58 mH
Grid source resistance	0.8929 Ω
Inverter frequency	10 kHz

In accordance with the grid-side inverter's control method, the DSSB regulator hysteresis control regulates the DC link voltage, while the q-axis current loop controller regulates the reactive power, and the d-axis current loop regulates the active power injection into the grid. Within the permitted working range of the regulator and the inverter, the DC link voltage is stabilized using the d-axis current loop of the grid-side inverter. Furthermore, as can be seen in Figure 22, it is possible to use a PI controller to use the VSI DC link voltage, V_{dc}, as a reference signal for the d-axis current because the DC link voltage, active power, and d-axis current of the grid-side inverter are directly correlated. The reference signal for the d-axis current of the grid is thus derived by comparing the DC link voltage with its reference signal produced by the DSSB regulator and via a PI controller.

Figure 29a–c show the performance of the front-loading inverter through the waveform of its phase and line voltages at the point of common coupling (V_f, V_{fL}), along with the grid variables (phase currents and voltages, dq-axis currents and voltages, and powers). It is demonstrated that the voltages and currents that are injected into the grid from the PMSG through the DSSB regulator and the VSI vary according to the variations in wind speed (10 m/s and 20 m/s) and the control strategies used for the suggested system.

The grid operates as an energy source because both of its types of power are negative. Since the reference value of the DSSB source current is applied at a constant 40 A, the grid's phase currents maintain a constant value of 100 A even in the presence of fluctuating wind speeds.

Figure 30a,b show the input/output DC powers of the DSSB, voltages, and currents, as well as the PMSG active and reactive powers that are injected into the grid through the VSI. Consequently, Figure 30c compares the active and reactive powers of all components of the proposed WECS. As Figure 30a illustrates, the hysteresis current-mode controller performs well because there is hardly any difference between the measured value of the source current, I_s, and its reference value, 40 A.

Furthermore, an equivalent amount of active power from the PMSG is converted to DC power within the DSSB regulator and then sent via the VSI to the grid system, which includes the LCL Kalman filters. As a result, the efficiency of the DSSB regulator is nearly 99%. Additionally, the PMSG reactive power is supplied into the grid system through the VSI with the help of the DSSB energy storage components.

The relationships between reactive powers and q-axis currents and active powers and d-axis currents are also evident. Furthermore, a negative or positive active or reactive power indicates that the corresponding WECS component is supplying or absorbing power. Nevertheless, whether the DSSB regulator is delivering P_o to the VSI or receiving P_s from the rectifier, its DC power (P_s or P_o) is always positive.

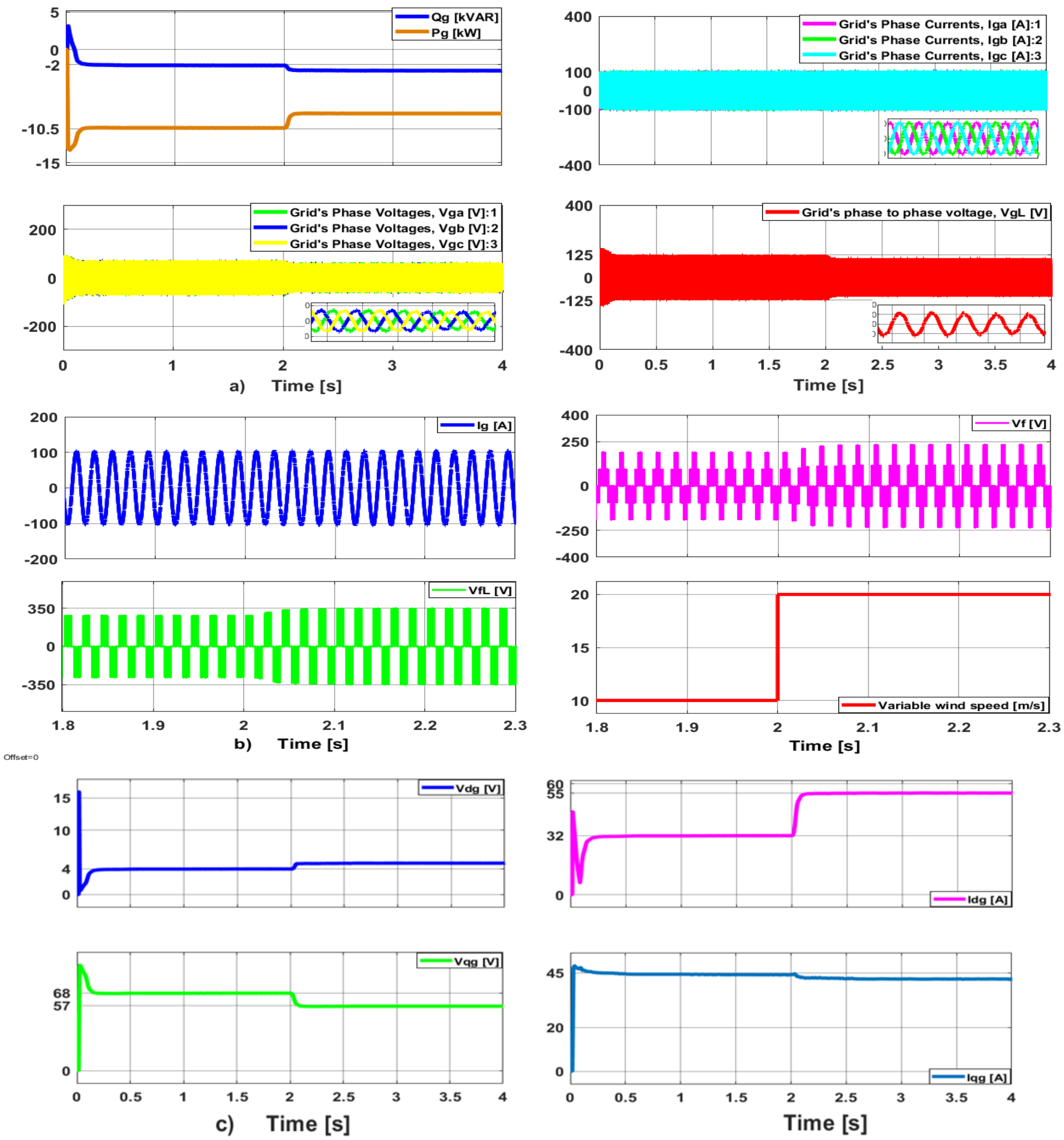

Figure 29. Responses of WECS variables (currents, line and phase voltages) to the step change in the wind speed profile from 10 m/s to 20 m/s: (**a**) waveforms of grid's phase currents (I_{ga}, I_{gb}, I_{gc}), phase voltages (V_{ag}, V_{bg}, V_{cg}), line voltage (V_{gL}), and active and reactive powers (P_g and Q_g); (**b**) a snapshot-waveform of VSI phase and line voltages (V_f, V_{fL}) and grid's phase current (I_g); (**c**) dq-axis phase currents and voltages of the grid.

Figure 31a shows how the wind speed variation from 10 m/s to 20 m/s affects the PMSG's electromagnetic torque, the mechanical torque generated by the turbine system, and the rotor angular speed. The system's hysteresis current-mode control technique that is implemented with the DSSB regulator keeps the PMSG torques constant, even when the wind speed varies from 10 m/s to 20 m/s.

Additionally, Figure 31b illustrates the PMSG's stator phase current (I_{gen}) and line voltage (V_{sL}) with their dq-axis phase currents and voltages, with a shorter-term snapshot of these variables given in Figure 31c. As shown within the yellow circle, in the d-axis current waveform of the PMSG, we can observe a short-term bump during the initial transient variation in the wind speed at 2 s. However, this does not affect the power exchange range since it happens for less than 0.02 s.

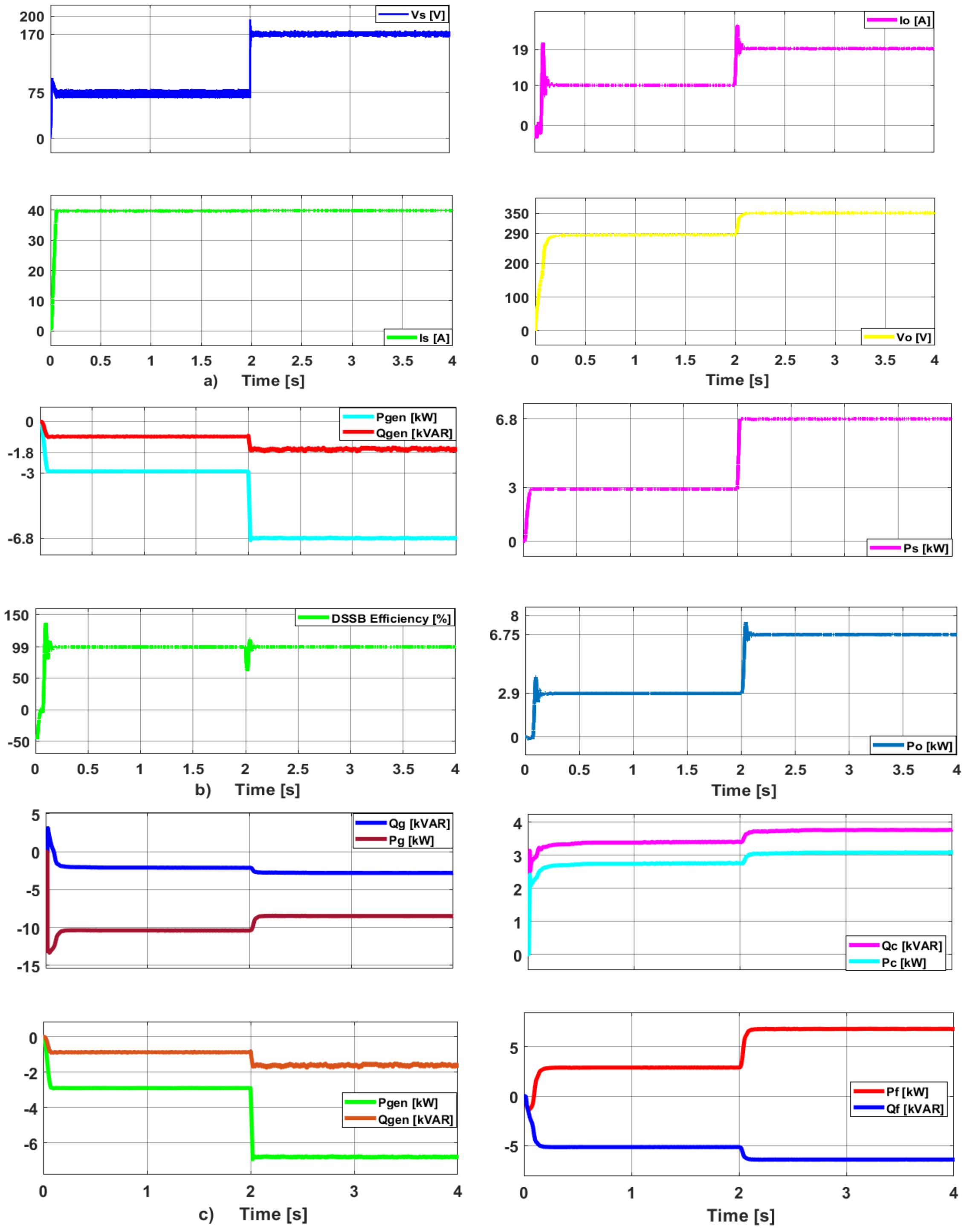

Figure 30. Simulation of WECS variables: (**a**) DSSB output/input currents and voltages as the wind speed changes from 10 m/s to 20 m/s. (**b**) DSSB output and input powers, P_s and P_o, and efficiency with PMSG's active and reactive powers. (**c**) Active and reactive power of all main WECS system components (grid, PMSG, DSSB, VSI).

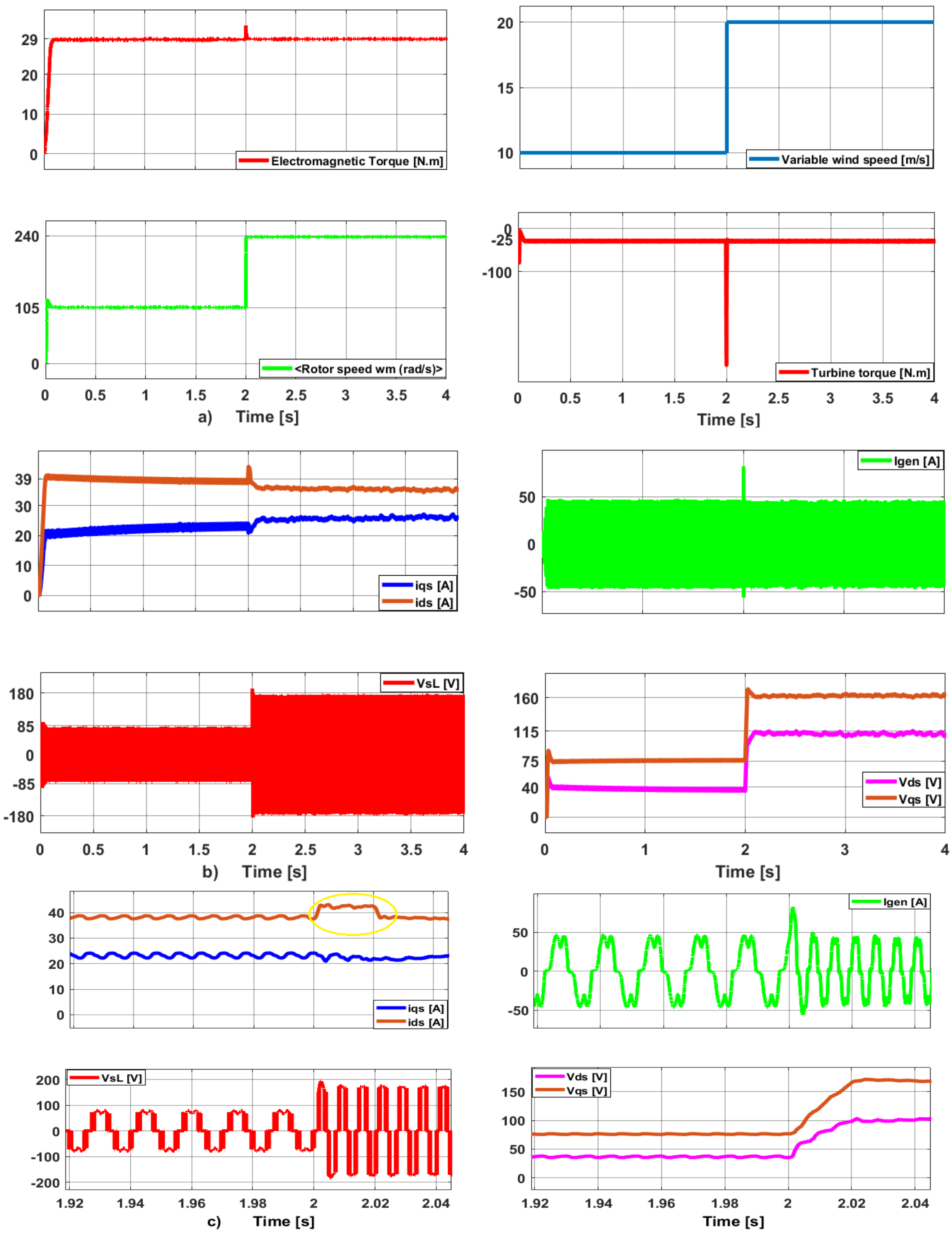

Figure 31. In response to a wind speed change from 10 m/s to 20 m/s, three types of PMSG variable waveforms are shown here: (**a**) PMSG torques and rotor angular speed; (**b**) PMSG stator phase current (Igen) and line voltage (VsL) with their dq-axis phase currents and voltages; and (**c**) a shorter-term snapshot of (**b**).

Reactive and active powers from the PMSG, LCL Kalman filters, and grid flow through the WECS system in opposite directions, and as they are used up by other system components, they are deducted from one another. The LCL transmission lines' shunt impedance

(RC) then absorbs the difference between these reactive and active power values as active power (P_c) and reactive power (Q_c). Furthermore, it is demonstrated that at a wind speed of 20 m/s, the reactive and active powers change noticeably in a stepwise manner in response to variations in wind speed. This aids in voltage drop compensation when the reactive powers in the system cancel each other out as the wind speed rises and falls. The suggested MPPT controller in combination with the hysteresis current-mode controller successfully controls the PMSG power at the necessary low reactive power and high active power values with the least amount of transient time. Consequently, the turbine's maximum power-point tracking power output is fed into the VSI as active power. The reactive power decreases in the direction of zero as the wind speed approaches the cut-out speed. In this configuration, the DSSB and VSI regulators function as a grid-side DC energy buffer for transients and the power fluctuations produced by the wind turbine, in addition to controlling active and reactive power [31–40].

Reactive power's exact compensation control is not considered in this paper. Numerous studies are looking into the parameters of the reactive power compensation mechanism and a control approach that incorporates reactive power compensation. Additionally, field-oriented control strategies based on advanced control theory still have a great deal of research value [38–40].

8. Conclusions

This research paper discusses a control strategy for a triple-phase voltage source inverter in a PMSG powered by a variable-speed wind system. It includes a thorough analysis, simulation using SIMULINK/MATLAB, and the use of a hysteresis current-mode-regulated DSSB regulator. While the control techniques discussed in this work are already established and widely used in research and control applications, the unique contributions of this study are as follows:

- A recently adopted hysteresis current-mode-controlled double-switch SEPIC–buck regulator (DSSB) with a dual-lead PI controller is examined and explained. This is achieved using mathematical analysis and simulation in SIMULINK/MATLAB.
- The main objectives of this are to compensate for wind speed variation-induced voltage instability and to track the maximum active power that can be injected into the series transmission line (LCL filter shunt impedance) from the grid and the PMSG using the hysteresis-regulated DSSB regulator.
- This paper also presents a dq current-controlled voltage source inverter (VSI) with two proposed PI controllers for current error elimination.
- To ascertain whether the performance of the front-loading VSI controller and DSSB regulator is satisfactory, the system performance is assessed under both normal and variable operating conditions as it is used to supply an AC triple-phase grid and a triple-phase RL. It is shown that the proposed WECS system with the DSSB regulator and VSI has very good control dynamic quality because it responds very accurately to step-change variations in the wind profile. MATLAB and Simplorer are used to verify the simulation.
- Additionally, the high performance of the recommended DSSB regulator during the turbine-side zero-wind-speed fault is demonstrated. During the zero-wind-speed fault, the DSSB source current and its output voltage—the VSI's DC link voltage—are maintained within a safe range. Every indicator falls between the typical ranges.
- Using the double-hysteresis current control in conjunction with the dq-current control of the voltage source inverter, the DSSB regulator tracks and regulates its input variables, and the voltage and current generated by the rectifier. Thus, the suggested DSSB regulator improves the monitoring of the maximum power point and efficiently maximizes the output power supplied to the load.

These simulation results indicate that the proposed hysteresis current-mode control has an excellent controlling effect on DSSB performance. The specific ways in which this is reflected are the MPPT technique, the reduction in DC link voltage fluctuation, and the recovery time following the fault.

Moreover, the simulation results show that the estimated and simulated values for the system parameters, such as DSSB voltage and current conversion, rotor and wind speeds, power, and torque, agree fairly well. Furthermore, the chattering effect of wind speed has no effect on the mechanical strain on the rotor shaft as the mechanical torque waveform of the PMSG remains constant despite variations in wind speed. The results of the simulation show that the control strategies with the DSSB regulator and VSI are sufficient, even with the variability in the wind speed profile.

Author Contributions: W.E.: Supervision, Writing, Acquisition, Validation, Investigation, Methodology, Conceptualization, Software, Formal Analysis, Resources, Data Curation, Visualization, Project Administration. M.A.: Validation, Investigation, Conceptualization, Publication Fee Acquisition. I.M.: Validation, Investigation, Conceptualization, Publication Fee Acquisition. All authors have read and agreed to the published version of the manuscript.

Funding: This research received no external funding.

Data Availability Statement: The original contributions presented in the study are included in the article, further inquiries can be directed to the corresponding author.

Acknowledgments: We genuinely appreciate the leadership and administration of Zarqa University that helped us to complete this research paper. The success of this research paper is greatly attributed to their financial support, professional advice, and guidance for conducting this research. The authors are grateful to Eng. Ali Emar's supports in methodology, conceptualization, writing, formal analysis, and software.

Conflicts of Interest: The authors declare no conflicts of interest.

References

1. Bin, W.; Lang, Y.; Zargari, N.; Kouro, S. *Power Conversion and Control of Wind Energy Systems*; John Wiley & Sons: Hoboken, NJ, USA, 2011. [CrossRef]
2. Emar, W.; Issa, H.; Kanaker, H.; Fares, O.; Attar, H. A New Double-Switch SEPIC-Buck Topology for Renewable Energy Applications. *Energies* **2024**, *17*, 238. [CrossRef]
3. Chinchilla, M.; Arnaltes, S.; Burgos, J.C. Control of permanent magnet generators applied to variable-speed wind energy systems connected to the grid. *IEEE Trans. Energy Convers.* **2016**, *21*, 130–135. [CrossRef]
4. Gajewski, P.; Pieńkowski, K. Advanced control of direct-driven PMSG generator in wind turbine system. *Arch. Electr. Eng.* **2016**, *65*, 643–656. [CrossRef]
5. Shadab, M.M.; Tariq, A. Performance analysis of PMSG connected with wind turbine. *Int. J. Adv. Technol. Eng. Res.* **2015**, *3*, 155–165.
6. Oner, Y.; Bekiroglu, N.; Ozcira, S. Dynamic Analysis of Synchronous generator with permanent magnets with Power Electronics. *Adv. Electr. Comput. Eng.* **2010**, *10*, 11–15. [CrossRef]
7. Emar, W.; Saraereh, O.A. Analytical and comparative study of different types of two-leg chopping up regulator. *Int. J. Adv. Comput. Sci. Appl.* **2019**, *10*, 5. [CrossRef]
8. Datta, S.; Deb, S.; Datta, A.; Adhikari, S.; Roy, B. Grid Connected PMSG Based Wind Energy Conversion System Using Back-to-Back Regulator. In *Intelligent Techniques and Applications in Science and Technology. ICIMSAT 2019*; Dawn, S., Balas, V., Esposito, A., Gope, S., Eds.; Learning and Analytics in Intelligent Systems; Springer: Cham, Switzerland, 2020; Volume 12. [CrossRef]
9. Yan, G.; Hu, W.; Jia, Q.; Liu, K.; Wang, J. Analysis of Subsynchronous Oscillation of Direct Drive PMSG Based Wind Farm under Low Operating Condition. *J. Electr. Eng. Technol.* **2021**, *16*, 1–13. [CrossRef]
10. Rahimi, M. Modeling, control and stability analysis of grid connected PMSG based wind turbine assisted with diode rectifier and boost regulator. *Int. J. Electr. Power Energy Syst.* **2017**, *93*, 84–96. [CrossRef]
11. Majout, B.; Bossoufi, B.; Karim, M.; Gaiceanu, M.; Livinti, P.; El Zair Laggoun, Z.; El Alami, H.; Majout, B. Comparative Analysis of Predictive and Direct Power Control Strategies for PMSG-Based WECS. In *Digital Technologies and Applications. ICDTA 2023*; Motahhir, S., Bossoufi, B., Eds.; Lecture Notes in Networks and Systems; Springer: Cham, Switzerland, 2023; Volume 669. [CrossRef]
12. Masters, G.M. *Renewable and Efficient Electric Power Systems*; John Wiley and Sons: Hoboken, NJ, USA, 2004.
13. Emar, W. Analysis, modeling, and simulation of step-up regulator using Matlab–Simulink and Simplorer. *Int. J. Model. Simul. Sci. Comput.* **2016**, *7*, 1650004. [CrossRef]
14. Emar, W. Analysis, Modeling and Control Design of a Synchronous Generator with a Wind Turbine and a Multilevel Voltage Source Inverter. *Int. J. Res. Electr. Electron. Eng.* **2015**, *3*, 1–15.

15. Chowdhury, M.M. Modelling and Control of Direct Drive Variable Speed Wind Turbine with Interior Permanent Magnet Synchronous Generator. Ph.D. Thesis, School of Engineering, University of Tasmania, Sandy Bay, TAS, Australia, 2014.
16. Chowdhury, M.M.; Haque, M.E.; Das, D.; Gargoom, A.; Negnevitsky, M. Modeling, parameter measurement and sensorless speed estimation of IPM synchronous generator for direct drive variable speed wind turbine application. *Int. Trans. Electr. Energy Syst.* **2015**, *25*, 1814–1830. [CrossRef]
17. Ragheb, M.; Ragheb, A.M. Wind Turbines Theory—The Betz Equation and Optimal Rotor Tip Speed Ratio. *Fundam. Adv. Top. Wind. Power.* **2011**, *1*, 19–38. [CrossRef]
18. Cui, P.; Zheng, F.; Zhou, X.; Li, W. Current harmonic suppression for permanent magnet synchronous motor based on phase compensation resonant controller. *J. Vib. Control* **2022**, *28*, 735–744. [CrossRef]
19. Gao, J.; Zhang, J.; Fan, M.; Peng, Z.; Chen, Q.; Zhang, H. Model Predictive Control of Permanent Magnet Synchronous Motor Based on State Transition Constraint Method. *Math. Probl. Eng.* **2021**, *2021*, 3171417. [CrossRef]
20. Emar, W.; Maher, R.A.; Jalil, A. Constant frequency digital hysteresis-band current controller for a three-phase voltage inverter. *Control Intell. Syst.* **2011**, *39*, 108. [CrossRef]
21. Agrawal, J.; Bodkhe, S. Steady-State Analysis and Comparison of Control Strategies for PMSM. *Model. Simul. Eng.* **2015**, *2015*, 306787. [CrossRef]
22. Emar, W. Hysteresis Current-Mode Regulated Modified SEPIC-Buck Regulator Used for Solar Photovoltaic Systems. *Arab. J. Sci. Eng.* **2024**, *49*, 7053–7077. [CrossRef]
23. Chacko, G.; Syamala, L.; James, N.; Jos, B.M.; Kallarackal, M. Switching Frequency Limited Hysteresis Based Voltage Mode Control of Single-Phase Voltage Source Inverters. *Energies* **2023**, *16*, 783. [CrossRef]
24. Xie, G.; Lu, K.; Dwivedi, S.K.; Rosholm, J.R.; Blaabjerg, F. Minimum-Voltage Vector Injection Method for Sensorless Control of PMSM for Low-Speed Operations. *IEEE Trans. Power Electron.* **2016**, *31*, 1785–1794. [CrossRef]
25. Errami, Y.; Ouassaid, M.; Maaroufi, M. A performance comparison of a nonlinear and a linear control for grid-connected PMSG wind energy conversion system. *Int. J. Electr. Power Energy Syst.* **2015**, *68*, 180–194. [CrossRef]
26. Davoodnezhad, R. Hysteresis Current Regulation of Voltage Source Inverters with Constant Switching Frequency. Ph.D. Thesis, RMIT University, Melbourne, VIC, Australia, January 2014.
27. Kim, Y.-S.; Chung, I.-Y.; Moon, S.-I. Tuning of the PI Controller Parameters of a PMSG Wind Turbine to Improve Control Performance under Various Wind Speeds. *Energies* **2015**, *8*, 1406–1425. [CrossRef]
28. Wu, Z.; Dou, X.; Chu, J.; Hu, M. Operation and Control of a Direct-Driven PMSG-Based Wind Turbine System with an Auxiliary Parallel Grid-Side Regulator. *Energies* **2013**, *6*, 3405–3421. [CrossRef]
29. Zhang, X.; Huang, C.; Hao, S.; Chen, F.; Zhai, J. An Improved Adaptive-Torque-Gain MPPT Control for Direct-Driven PMSG Wind Turbines Considering Wind Farm Turbulences. *Energies* **2016**, *9*, 977. [CrossRef]
30. Iqbal, A.; Moinoddin, S.; Reddy, B.P. *Electrical Machine Fundamentals with Numerical Simulation Using MATLAB/SIMULINK*; Wiley: Hoboken, NJ, USA, 2021.
31. Mohamed, R.; Mossa, M.A.; El-Gaafary, A. Performance Enhancement of a Variable Speed Permanent Magnet Synchronous Generator Used for Renewable Energy Application. *Int. J. Robot. Control Syst.* **2023**, *3*, 530–560. [CrossRef]
32. Douglass, P.J.; Trintis, I. Balancing distribution systems with three-phase active front end rectifiers: Field experiment results. *IET Gener. Transm. Distrib.* **2017**, *11*, 3749–3755. [CrossRef]
33. Yazdani, A.; Iravani, R. *Voltage-Sourced Regulators in Power Systems: Modeling, Control, and Applications*; Wiley-IEEE Press: Hoboken, NJ, USA, March 2010; 464p, ISBN 978-0-470-52156-4.
34. da Costa, I.D.L.; Brandao, D.I.; Seleme, S.I., Jr.; Morais, L.M.F. Torque Control for PMSGBased Wind-Power System Using Stationary abc-Reference Frame. *Energies* **2022**, *15*, 8060. [CrossRef]
35. Wu, F.; Liu, R.; Xie, Y.; Lyu, J. A modified power decoupling control strategy for a grid-connected inverter with a low switching frequency under unbalanced grid voltages. *Energy Rep.* **2022**, *8* (Suppl. 5), 757–768. [CrossRef]
36. Gannoun, M.; Naouar, M.W.; Monmasson, E. Modeling of a PMSG-based wind turbine assisted by a diode rectifier. In Proceedings of the 2019 International Conference on Signal, Control, and Communication (SCC), Hammamet, Tunisia, 16–18 December 2019.
37. Ravi, T.; Kumar, K.S.; Dhanamjayulu, C.; Khan, B.; Rajalakshmi, K. Analysis and mitigation of PQ disturbances in grid-connected systems using fuzzy logic-based IUPQC. *Sci. Rep.* **2023**, *13*, 22425. [CrossRef] [PubMed]
38. Zholtayev, D.; Rubagotti, M.; Do, T.D. Adaptive super-twisting sliding mode control for maximum power point tracking of PMSG-based wind energy conversion systems. *Renew. Energy* **2022**, *183*, 877–889. [CrossRef]
39. Salime, H.; Bossoufi, B.; Motahhir, S.; El Mourabit, Y. A novel combined FFOC-DPC control for wind turbine based on the permanent magnet synchronous generator. *Energy Rep.* **2023**, *9*, 3204–3221. [CrossRef]
40. Tao, R.; Wu, M.; Ying, G.; Tang, J.; An, R.; Wang, Q.; Liu, J. A phase compensation method combined with power correction for suppressing sub-synchronous resonance of wind generation under weak grid. *Int. J. Electr. Power Energy Syst.* **2023**, *151*, 109115. [CrossRef]